# Predicting longitudinal brain atrophy in Parkinson's disease patients using an agent-based model

**Alaa Abdelgawad**

Faculty of Medicine

Integrated Program in Neuroscience,

McGill University, Montreal

June 2021

A thesis submitted to McGill University in partial fulfillment of the requirements of the degree of Master of Science.

# Table of Contents

# 1. Abstract

Several studies support that alpha-synuclein (aSyn) pathology transfers in a prion-like behavior via axonal projections. However, the mechanism that translates aSyn pathology spread to disease progression in Parkinson's disease (PD) remains unknown. Here, we investigated the atrophy progression pattern in a longitudinal dataset of PD patients seen at baseline, one, two, and four years of follow-up. Then, we applied the agent-based Susceptible-Infected-Removed (SIR) dynamic model to simulate the spread of misfolded aSyn. We demonstrate three main findings. First, atrophy was significantly progressed over four years in subcortical and cortical regions based on deformation-based morphometry maps extracted from T1-weighted MRI data. Second, the SIR model recapitulated *in silico* the spatiotemporal distribution of atrophy observed in the PD longitudinal dataset. Third, SIR rewired, repositioned and genetic null models revealed the significant role of connectome topology, geometry, and regional gene expression of both SNCA and GBA in shaping disease spread longitudinally in PD. Altogether, these results demonstrated that the SIR model is a promising tool for modeling multifactorial neurodegenerative diseases over time.

## 2. Resume

Plusieurs études supportent l'hypothèse que l'alpha-synucléine pathologique se propage à travers le cerveau par l'entremise des fibres axonales à la manière d'un prion. Cependant, les mécanismes qui expliquent la propagation de l'alpha-synucléine pathologique dans la maladie de Parkinson demeurent encore mal compris. Dans cette étude, nous avons premièrement étudié la progression de l'atrophie cérébrale dans une cohorte longitudinale de patients avec une maladie de Parkinson suivis sur quatre ans. Nous avons ensuite utilisé un modèle compartimental Susceptible-Infecté-Rétabli/Retiré (SIR), implémenté comme un modèle computationnel basé sur l'agent, pour simuler la propagation de l'alpha-synucléine pathologique dans le cerveau. Ce faisant, trois observations majeures ont pu être faites. Premièrement, l'atrophie mesurée dans le cerveau des participants grâce à la morphométrie basée sur la déformation progresse significativement dans les régions corticales et sous-corticales sur une période de 4 ans. Deuxièmement, le modèle computationnel SIR réplique in silico le patron de distribution spatiotemporel d'atrophie observé dans la cohorte longitudinale. Troisièmement, la génération de modèles nuls dans lesquels ont été randomisées soit la connectivité cérébrale soit l'expression génétique révèle qu'autant la topologie et la géométrie du connectome que l'expression régionale de SNCA et de GBA façonnent la propagation de la maladie de Parkinson dans le temps. Ces résultats démontrent que le modèle computationnel SIR s'avère un outil prometteur pour modéliser la progression des maladies neurodégénératives selon une perspective multifactorielle.

## 3. Acknowledgment

First, I would like to express my deep and sincere gratitude to my supervisor Dr. Alain Dagher for his guidance and mentorship. Without his immense assistance and support, my thesis work would not have been possible today. Thanks to my committee members Dr. Bratislav Misic and Dr. Jean-Baptiste Poline for their help and suggestions.

Special thanks to Dr. Shady Rahayel for his huge guidance in data analysis, manuscript creation and providing neat French translation of my abstract. I would also like to thank everyone else in Dr. Dagher's lab for creating a friendly working environment especially online during the pandemic.

I am also grateful for the financial support I received from the Jeanne-Timmins Costello Fellowship and IPN recruitment award. Finally, Thanks to my parents and sisters for their emotional support and constant encouragement.

## 4. Contribution of Co-authors

I declare that I have performed the major work in method implementation, data processing and analysis, and writing manuscript. The following highlights the contribution of my co-authors.

*Shady Rahayel, PhD*, was involved in conceptualization, methodology, and reviewing manuscript.

*Ying-Qiu Zheng, MSc*, *Christina Tremblay, PhD*, and *Andrew Vo*, PhD were involved in methodology.

*Bratislav Misic, PhD*, was involved in conceptualization and supervision.

*Alain Dagher, MD PhD* was involved in conceptualization, reviewing manuscript, funding, and supervision.

# 5. INTRODUCTION

## 5.1. Parkinson's disease progression

Parkinson's disease (PD) is the second most prevalent neurodegenerative disease following Alzheimer's disease. As PD progresses over time, different motor and non-motor symptoms develop which vary in occurrence, onset, severity, and rate of progression. The major motor symptoms in PD are tremor, rigidity, bradykinesia, and postural instability (Hughes et al. 1992; Postuma et al. 2015), while non-motor symptoms include but are not limited to sleep disturbances, autonomic dysfunction, depression, and dementia. The abovementioned symptoms are expected to manifest and progress in PD patients during their course of the disease (Poewe et al., 2017). Therefore, there is an unmet need for a tool that can assess PD progression efficiently and accurately. Currently, two main hypotheses can facilitate the development of such a tool: the Braak staging hypothesis and local selective vulnerability.

PD is characterized by the pathological intracellular aggregation of misfolded alpha-synuclein (aSyn) into Lewy bodies and neurites (Dickson et al., 2009; Spillantini et al., 1997). In the brain, these deposits appear in a stereotypical fashion, emerging in the olfactory bulb and caudal brainstem and then ascending towards the midbrain, limbic areas, and cerebral cortex (Braak et al., 2003; Braak et al., 2004). This spatiotemporal distribution patterns of pathology have led to the hypothesis that misfolded aSyn may harbor prion-like properties (Brundin and Melki, 2017), allowing it to spread between cells and impose its misfolded conformation onto native endogenous, otherwise normal aSyn proteins from the recipient cell (Peng et al., 2020). Several studies have investigated the prion-like behavior of pathological aSyn in animal models and have provided direct evidence for pathological templating and between-cell dissemination of pathology (Peng et

al., 2020). Indeed, the injection of synthetic aSyn preformed fibrils or brain lysates from patients with a synucleinopathy has demonstrated the local formation of aSyn pathology and its propagation through brain networks in wild-type and transgenic mice, rats, and non-human primates (Henrich et al., 2020; Luk et al., 2012a; Luk et al., 2012b; Masuda-Suzukake et al., 2013; Rey et al., 2018; Rey et al., 2016; Watts et al., 2013). In humans, the evidence for a prion-like behavior of pathological aSyn has so far been indirect. For instance, in patients who received fetal mesencephalic neuronal transplants, Lewy-related pathology could be observed inside cells that were grafted a decade earlier (Kordower et al., 2008; Li et al., 2008), suggesting that pathology spread to the grafts from the surrounding milieu. Some other findings, not always replicated, also reported that patients who underwent vagotomy had a lower risk of developing PD, possibly due to the interruption of the transmission of pathology from the gut to the brain (Liu et al., 2017; Svensson et al., 2015). Also, using MRI-derived volume deformation and cortical thinning as proxy measures of tissue atrophy, the pattern of brain changes observed in *de novo* PD patients was shown to significantly overlap with the brain's connectivity pattern (Yau et al., 2018; Zeighami et al., 2015).

Although important, other studies have also demonstrated that the distribution of aSyn pathology was not solely explainable by the brain's synaptic connectivity pattern and that other cell-autonomous factors appear to play a key role in driving the generation of aSyn pathology in the brain (Gonzalez-Rodriguez et al., 2020; Henrich et al., 2020; Surmeier et al., 2017). This was supported by findings in mice of certain cell types being more vulnerable to the disease process and by the dose-dependent accumulation of pathology occurring in patients with duplications and triplications of the SNCA gene (Chartier-Harlin et al., 2004; Ibanez et al., 2004). In addition,

mutation in the GBA gene which encodes for the lysosomal enzyme glucocerenrosidase was found to be involved in SNCA accumulation and development of PD and other Lewy body disorders (Du et al.,2015). Nonetheless, the mechanisms underlying the propagation of pathological aSyn in PD remain unclear.

### 5.2. Network-based modeling of neurodegeneration

One way to better understand the mechanisms underlying aSyn spread in PD is through Network-based modeling, which can be categorized into diffusion models and epidemic models. Both categories are based on the current evidence of prion-like misfolded proteins propagating through neurons via synaptic transmission. In diffusion models, the spreading of misfolded proteins is deterministic and modeled with series of partial differential equations (Raj et al., 2012; Henderson et al., 2019). Such models are relatively simple mathematically and solved either by finite element method on the whole brain or by graph Laplacian on brain network (Weickenmeier et al,2018a; Raj et al., 2012). Diffusion models are limited in their applications due to the assumption that disease spread follows concentration gradient, which is not biologically true. Moreover, diffusion models do not consider the dynamic synthesis and clearance of infection and selective vulnerability of regions.

Epidemic models have shown promising potential in recapitulating the accumulation and propagation of neurodegenerative disease spread. Several epidemic models have been suggested. The standard epidemic approach is the full-mixed model, in which contact is possible at some level with the entire population given a transmission rate. However, this is an unrealistic assumption

since sufficient contact between two individuals in the entire population is small enough to be negligible. With advanced epidemic models such as SI, SIR, and SIS (S for susceptible, I for infected, R for recovered), stochasticity is introduced considering model parameters and network of the disease (Newman et al, 2010). The inherent randomness with stochastic models allows for the interaction between various parameters resulting in better outcomes. Epidemic methods consider nodes (e.g., vertices, regions) on the graph as hosts where disease is initiated in one node (epicenter) and develops into a large outbreak on the network (Britton et al, 2020). Throughout the epidemic process, the hosts adapt to different states: infected, susceptible, or recovered- in the case of the SIR model. Although these classic epidemic models have been of great success in modeling different epidemics, they failed to effectively model spatial aspects as well as explicit individual behavior among others in the system. Therefore, the agent-based model has the advantage in such cases (Di Stefano et al 2000, Frias-Martinez et al 2011). For neurodegeneration modeling, an agent represents protein which can get affected if encounters misfolded protein, and if so, the misfolded protein serves as a template to infect other susceptible agents throughout brain connectome.

In this study, we extended the use of a recently developed agent-based SIR model (Zheng et al, 2019) on a longitudinal PD dataset that incorporated volumetric information extracted from T1-weighted MRI images. The Next section will discuss neuroimaging techniques used in PD studies to extract related morphometric changes.

### 5.3. Neuroimaging in PD

The major roles of neuroimaging include providing accurate and timely diagnosis, evaluating treatments designed to mitigate symptoms, and monitoring disease progression (Mohammed et al,

2019). Neuroimaging studies using magnetic resonance imaging (MRI), single-photon emission computed tomography (SPECT), and positron emission tomography (PET) have provided a deep understanding of PD-related changes. PET and SPECT report brain changes at the molecular level using ionizing radioactive, while MRI detects directly or indirectly structural and functional brain alterations using magnetic fields and radio waves (Politis et al 2014). Here, we used T1-weighted MRI brain images to study structural changes longitudinally in PD patients. Morphometric MRI analysis (e.g., regional shape, volume, and thickness) has demonstrated potential for diagnostic purposes in neurodegenerative disorders. Morphometric methods include volumetric-based (e.g., voxel-based morphometry (VBM) and deformation-based morphometry (DBM)) and surface-based (e.g., cortical thickness) approaches (Ad-Dab'bagah et al, 2005; McCarthy et al, 2018).

Here, we studied the longitudinal changes in cortical and subcortical regions. Since Cortical thickness analysis does not detect subcortical changes (Pereira et al., 2014), a volumetric-based approach was used in specific DBM, which has more sensitivity than VBM. For VBM, T1-weighted images are linearly registered to a template (Lin, C et al 2013). The template can be either an average image of the study population or a standard unbiased template of normal individuals such as the Montreal Neurological Institute brain templates (e.g., MNI-ICBM-152) (Fonov et al., 2009, 2011). The Next step includes automated segmentation of the registered image into gray and white matter and cerebrospinal fluid (CSF), followed by spatial normalization on the gray matter maps to quantify gray matter density across subjects. Similarly, DBM registers the T1-weighted MRI to the template but non-linearly, matching brain distribution of gray and white matter and CSF based on similarities of intensities and contrast. Unlike VBM, the non-linear registration of DBM requires no previous knowledge of brain segmentation allowing for better and

more sensitive detection of subtle differences (Borghammer et al 2012). After registration, DBM estimates the displacement value at each voxel generating a field of vectors that measure the amount each voxel moved from the template to match the individual subject's image. The Jacobian determinant of displacement matrix is calculated to estimate the local volumetric change whether it is atrophy or expansion (Zeighami et al., 2015).

In addition, image preprocessing in structural MRI is necessary proceeding any further analysis such as registration or morphometric analysis. Preprocessing steps are important for better detection and increasing the signal-to-noise ratio of T1-weighted MRI images. The common preprocessing steps include motion and intensity non-uniformity correction, intensity normalization, and noise reduction. Motion correction aims towards correcting image distortion due to the movement of the subject in the scanner, while intensity non-uniformity correction measures the bias resulting from the scanner's non-uniform static magnetic field. Noise reduction minimizes noise while keeping relevant information about brain structure and anatomical alterations intact (Park et al, 2019). Finally, intensity normalization is commonly used to handle biases in multi-center studies where images have a large range of intensities; histogram-based normalization is the general technique used on MRI images collected with different acquisitions (Madabhushi et al, 2006).

### 5.4. Review of PD studies using morphometric approaches

This section briefly summarizes related findings in the literature that used morphometric approaches to study PD-related changes. Several studies applied morphometric analysis besides other imaging and clinical measures to investigate disease classification and subtypes. Using DBM

along with other data modalities, a recent study by (Markello et al. 2020) characterized heterogeneity in PD by integrating multimodal data of morphometric, molecular, and clinical measures. They used similarity network fusion, an unsupervised learning method, to derive patients' subgroups from integrated data maps. Data used was obtained from 183 de novo PD patients from the Parkinson's Progression Markers Initiative (PPMI). Another recent study by (Martins et al. 2021) aimed for developing an automated classification system comparing three classes: control, idiopathic Parkinson's disease, and atypical Parkinsonian. Their classification algorithm was based on a linear support vector machine classifier using imaging-extracted features. The classifier combined grey matter volumetric data with distribution volume ratio (DVR) of PET data, which quantifies tracer binding to D2/D3 receptors in subcortical regions. They reported higher classification accuracy (79.9%) combining gray matter morphometry and DVR together.

Other studies focused on morphometric methods to investigate disease pathology progression in PD. (Zeighemi et al. 2019) has reported that PD-network atrophy pattern, based on DBM, is a better predictor of progression than biomarkers that measures dopaminergic deficit. They showed that the MRI-biomarker of atrophy had a higher accuracy score (AUC=0.63) than more specific biomarkers such as DAT SPECT and MRI-measure of substantial nigra. This study considered 362 drug-naiive early-stage PD patients from PPMI. Investigating structural changes, (Borghammer et al. 2010) observed a significant reduction in the left cerebellum in early-stage PD as to Control using DBM. In line with another VBM study, PD patients showed significant atrophy in the cerebellum bilaterally compared to controls (Camicioli et al. 2009). In addition, they observed an association between grey matter atrophy in limbic areas and deficits in memory and

executive functions. Reduction in grey matter volume in the putamen, prefrontal cortex, parahippocampal gyrus, and the bilateral caudate nucleus has also been observed in PD patients (Nagano-Saito et al 2005; Cui et al, 2020).

### 5.5. Thesis overview

In this study, we measured the progression of atrophy in PD patients over one, two, and four years and applied the agent-based SIR Model to assess if SNCA and GBA gene expression and structural features of the connectome significantly contributed to recreating the atrophy patterns. Additional analyses were performed to assess if the patterns generated in silico overlapped with the Braak staging scheme. We found that the agent-based SIR Model accurately recreated the atrophy observed longitudinally in PD and that both gene and connectivity are significant contributors to atrophy.

## 6. METHODS

### 6.1. Participants

A total of 631 patients with de novo PD and 157 healthy controls were included from the PPMI database (www.ppmi-info.org). The PPMI is a longitudinal observational international study aimed at assessing progression markers of PD and includes a comprehensive set of clinical and MRI measures acquired in patients with de novo PD and healthy controls (Marek et al., 2018). To be included in the PPMI, PD patients: 1) had at least two features among resting tremor, bradykinesia, and rigidity or either asymmetric resting tremor or asymmetric bradykinesia, 2) had a diagnosis of PD for less than two years, 3) had a baseline Hoehn and Yahr stage of I or II, 4) had

a dopamine transporter binding deficit confirmed using SPECT scan, 5) were not expected to require medications for PD within six months from the baseline assessment, 6) were at least 30 years old, and 7) did not have dementia. For healthy controls, a Montreal Cognitive Assessment (MoCA) score below 27 or a first-degree relative with a clinical diagnosis of idiopathic PD led to exclusion. The longitudinal follow-up of PPMI now extends to around 5 years; for this study, only the participants with MRI acquisition performed at baseline and either one, two, and/or four years were considered for analysis due to the limited number of scans acquired 3 (i.e., 3 participants) and 5 years (i.e., 2 participants) after baseline.

## 6.2. MRI

### 6.2.1. MRI acquisition

T1-weighted MRI brain images were acquired at different sites across the United States, Canada, and Europe. The acquisition protocols are available on the PPMI study (http://www.ppmi-info.org/study-design/research-documents-and-sops/) with the following parameters: repetition time (TR) = 2,300 ms; echo time (TE) = 2.98 ms; field of view (FOV) = 256 mm; flip angle = 9; and voxel size = 1 $mm^3$.

### 6.2.2. Deformation-based morphometry

Deformation-based morphometry (DBM) was performed on the baseline and longitudinal T1-weighted scans of PD patients and controls to derive whole-brain individual maps representing the deformation needed for a voxel to be normalized to the template space. DBM was done using the default parameters available in the CAT12 toolbox in SPM12 (www.neuro.uni-jena.de/cat). This resulted in a set of processed image files for each participant that included a voxel-wise whole-

brain map of Jacobian determinants, which was used as the measure of local brain tissue atrophy after the application of a 4 mm full width at half maximum isotropic smoothing kernel. Images were visually inspected at each step and excluded if abnormal or if the automated quality rating was below 80%.

### 6.2.3. Brain parcellation

The normalized smoothed Jacobian determinants maps were next parcellated using a previously used atlas made of 42 cortical and subcortical brain regions for which regional *SNCA* and *GBA*, as well as structural connectome features were available (Zheng et al., 2019). This atlas included 34 cortical regions derived from the Desikan-Killiany atlas and 7 subcortical regions, namely the putamen, caudate, pallidum, thalamus, hippocampus, amygdala, and accumbens, available as part of the FreeSurfer processing stream (http://surfer.nmr.mgh.harvard.edu) (Desikan et al., 2006). Due to its importance in PD, the substantia nigra was additionally included based on the segmentation available from the 7-tesla MRI "Atlasing of the basal ganglia" Atlas (https://www.nitrc.org/projects/atag) (Keuken et al., 2014). Using FLIRT (https://fsl.fmrib.ox.ac.uk/fsl/fslwiki/FLIRT), the 42-region atlas was then linearly registered to the individual deformation maps and a set of 42 regional deformation values were extracted for each image using the MarsBaR region of interest toolbox for SPM (https://marsbar.sourceforge.net). Note that the atlas only included regions from the left hemisphere due to the *SNCA* and *GBA* gene expression for the right hemisphere being available for only 2 of the 6 post-mortem brains included in the Allen Human Brain Atlas (AHBA) (Hawrylycz et al., 2012) and also due to possible errors associated with the detection of

interhemispheric connections during the deterministic streamline tractography protocol (see below).

### 6.2.4. Regional atrophy standardization

A W-scoring approach was then performed to correct for the normal effects of age and sex on the brain (La Joie et al., 2012; Tremblay et al., 2021). The regional deformation values from each PD patient's image were converted into age- and sex-corrected W-scores based on the values observed in the 157 controls available at baseline. There was no significant difference in age and sex between the controls (age: 60.1± 11.9; 66% male) at baseline and the PD group (BL age: 60.9± 10; 63% male – Y1 age: 60.9 ± 9.3; 63% male – Y2 age: 60.9 ± 9.3; 63% male – Y4 age: 64.4 ± 9.9; 69% male) at each time point. Only the values from controls seen at baseline were used for standardization due to the limited number of controls who underwent MRI during follow-up. The standardization formula was:

$$Wscore = \frac{PD_{raw\ value} - PD_{predicted\ based\ on\ HC}}{SD_{residuals\ in\ HC}}$$

where the predicted value for a PD patient based on control data was given by ($\beta_1$*age + $\beta_2$*sex + $\beta_3$). In other words, this yielded regional deformation values that represented the difference in W scores between a PD patient's deformation value and the deformation value that is expected for the patient's age and sex. The individual W-scores were next averaged between patients for a given region, resulting in a set of 42 regional W-scores for baseline and each of the three follow-up time points. The average W-scores seen at each follow-up time point was then subtracted from those observed at baseline to yield a W-score difference over time (i.e., atrophy progression over one, two, and four years). A negative W-score difference represented atrophy progression in PD

patients, whereas a positive W-score indicated volume expansion in patients during follow-up. The three sets of 42 atrophy difference values, one for the difference between baseline and every follow-up time point, were the observed patterns of atrophy progression to which was compared the pattern of simulated atrophy generated *in silico* by the agent-based SIR Model.

## 6.3. Agent-based SIR Model

### *6.3.1. Overview of the model*

The agent-based SIR Model simulates the brain spread of aSyn based on *SNCA* and *GBA* gene expression and structural features of the connectome (Zheng et al., 2019). In this model, the synthesis and degradation of aSyn agents are modulated by the local expression of *SNCA* and *GBA*, respectively. Every agent can belong to one of three compartments: "Susceptible" when representing the normal protein, "Infected" when representing the misfolded protein, and "Removed" when the protein gets degraded or spreads to another region. Every Susceptible agent can turn into an Infected agent when it encounters an Infected agent in a region. Both Susceptible and Infected agents have a probability of either being degraded inside a region or spread to a connected area. whereas the probability of spreading to another region is based on the strength of the connectivity between the source and the target regions.

The model is run by first initiating pathology inside a seed region, here the substantia nigra, and simulating the spread over a total of 10,000 iterations. At each iteration, a simulated atrophy value is generated for every region that is based on the local accumulation of infected agents (i.e., toxic event) and the effect of deafferentation (i.e., cell loss). To investigate how well the parameters of the spreading model replicated the progression of atrophy in PD, the spread was simulated with

the same 42-region atlas used for the MRI-derived observed patterns of atrophy. This allowed comparing the pattern of regional values of simulated atrophy to the patterns of atrophy progression observed between baseline and one, two, and four years. In other words, following the initiation site/epicenter of pathology into the substantia nigra, the model used local information about the connectome's architecture and the regional gene expression to modulate the behavior of aSyn in the brain and to simulate local accumulation of aSyn pathology and atrophy. The model was implemented into five different modules, namely the production of normal aSyn, the clearance of normal and misfolded aSyn, the misfolding of normal aSyn, the propagation of normal and misfolded aSyn, and the accrual of atrophy (see below for details about each module).

#### *6.3.2. Production of normal aSyn*

In the model, the synthesis of aSyn inside every region was modulated based on the regional gene expression of *SNCA*, which was extracted for the 42 regions based on six post-mortem brains available as part of the AHBA (Hawrylycz et al., 2012). The values were averaged across samples to yield an expression vector of synthesis that was inserted back into the model (see Zheng et al., 2019). The synthesis rate in a region $i$ per unit time occurred with probability $\alpha_i$:

$$\alpha_i = \boldsymbol{\Phi}_{0,1}(SNCA\text{expression}_i)$$

where $\boldsymbol{\Phi}_{0,1}(\cdot)$ was the normal cumulative distribution function of *SNCA* expression in region $I$, with a higher value representing a higher regional aSyn synthesis rate. The increment of normal agents in region $i$ was given by $\alpha_i S_i \Delta t$, where $\Delta t$ was the total time and $S_i$ was the region size. The

time increment used for the main analyses was set at $\Delta t = 0.1$, but peak correlation fits were robust with values from 0.1 to 0.9 (Figure 6).

### *6.3.3. Clearance of normal and misfolded aSyn*

Likewise, the degradation of aSyn inside every region was modulated based on the regional gene expression of *GBA*, which was also extracted from the AHBA. The clearance rate of both normal and misfolded agents in region *i* per unit time occurred with probability $\beta_i$:

$$\beta_i = \boldsymbol{\Phi}_{0,1}(\text{GBAexpression}_i)$$

where $\boldsymbol{\Phi}_{0,1}(\cdot)$ was the normal cumulative distribution function of *GBA* expression in region *i*. The probability of an agent still being active after total time $\Delta t$ was given by $lim_{\delta\tau \to 0}(1 - \beta\delta\tau)^{\Delta t/\delta\tau} = e^{-\beta\Delta t}$. In other words, as the degradation rate increased, the probability of an agent remaining active in the region decreased. Accordingly, the proportion of cleared agents within timestep $\Delta t$ was $1 - e^{-\beta\Delta t}$.

### *6.3.4. Misfolding of normal aSyn (infection transmission)*

Infected agents had the ability to impose their abnormal template onto susceptible agents and turn them into infected agents. The probability of a susceptible agent that survived clearance of not being infected corresponded to $(1 - \gamma_i^0)^{M_i}$, where $M_i$ was the population of infected agents in region *i* and $\gamma_i^0$ was the baseline likelihood that a single misfolded agent turned a susceptible agent into an infected agent. The baseline likelihood $\gamma_i^0$ was given by $1/S_i$, where $S_i$ was the region size. Accordingly, the probability per unit of time that a susceptible agent surviving clearance in region

*i* turned into an infected agent due to the action of at least one of the $M_i$ infected agents present in region *i* was given by $\gamma_i = 1 - e^{M_i ln(1-\gamma_i^0)}$. Like the previous module, the probability that a susceptible agent remained susceptible after total time $\Delta t$ was given by $lim_{\delta\tau \to 0}(1-\gamma_i^0 \delta\tau)^{M_i \Delta t/\delta\tau} = e^{-\gamma_i^0 M_i \Delta t}$, whereas the probability that a susceptible agent became infected after total time $\Delta t$ was given by $1 - e^{-\gamma_i^0 M_i \Delta t}$. As a result, the increment of the population of normal proteins $N_i$ in region *i* occurred with:

$$\Delta N_i = \alpha_i S_i \Delta t - (1 - e^{-\beta_i \Delta t}) N_i$$

Once the system reached the stable point, the populations of susceptible ($N_i$) and infected agents ($M_i$) were respectively updated as followed:

$$\Delta N_i = \alpha_i S_i \Delta t - \left(1 - e^{-\beta_i \Delta t}\right) N_i - (e^{-\beta_i \Delta t})(1 - e^{-\gamma_i^0 M_i \Delta t}) N_i$$

$$\Delta M_i = \left(e^{-\beta_i \Delta t}\right)\left(1 - e^{-\gamma_i^0 M_i \Delta t}\right) N_i - (1 - e^{-\beta_i \Delta t}) M_i$$

### *6.3.5. Propagation of normal and misfolded aSyn*

Every susceptible and infected agent had a probability to spread outside the region to other brain regions. To implement this, the structural connectivity matrix created previously for the 42-region atlas was used (see Zheng et al., 2019). Briefly, the structural connectivity matrix was created using 1,027 preprocessed diffusion-weighted and T1-weighted MRI images from the Human Connectome Project (2017 Q4; 1,200-subject release). The diffusion data were reconstructed onto the individual T1-weighted images using generalized q-sampling imaging. Voxel-wise

quantitative anisotropy and the spin distribution function were measured to assess the density of water diffused in different directions. Deterministic streamline tractography was then performed for each region using DSI Studio (www.nitrc.org/projects/dsistudio), resulting in 100,000 streamlines per region with the following parameters: angular cut-off of 55, step size of 0.5 mm, minimum length of 20 mm, and a maximum length of 400 mm. The density of streamlines between every two regions represented the connectivity strength between the seed and target region normalized by the target region voxel size and mean length of streamlines, compensating for the biases induced by differences in region size and by longer fibers.

To account for the mobility pattern of an agent between regions, we used a distance matrix and a structural connectivity matrix. The distance matrix was constructed by calculating the Euclidean distance of corresponding streamlines. For the structural connectivity matrix, a connection profile based on the density of streamlines was created for each region with self-connection set to 0; then concatenated to form a 42x42 structural connectivity matrix for each subject. Finally, a group-consensus approach was adopted by averaging 35 % of the most commonly occurring edges across all subjects to generate one group-level structural connectivity matrix. To test the robustness, the analyses were also performed using different matrix densities, namely using the 30% and 40% of most occurring edges (Table 3).

Using the matrix of structural connectivity, every agent could either remain in region *i* or enter the edges via fiber tracts with probabilities:

$$P_{region_i \rightarrow region_i} = \rho_i$$

$$P_{region_i \to edge_{ij}} = (1 - \rho_i) \frac{w_{ij}}{\sum_j w_{ij}}$$

where $w_{ij}$ was the undirected connection weight between region *i* and region *j* and $\rho_i$ was the probability of an agent to remain in region *i*. This probability was set to 0.5 for every region. The variations in $\rho_i$ led to a negligible difference when recreating atrophy (Figure 6). Likewise, both susceptible and infected agents could exist in an edge *(i,j)* per unit time with binary probabilities:

$$P_{edge_{i,j} \to region_j} = \frac{1}{l_{i,j}}$$

$$P_{edge_{i,j} \to edge_{i,j}} = 1 - \frac{1}{l_{i,j}}$$

where $l_{ij}$ was the length of the edge between regions *i* and *j*. The increments in $N_i$ and $M_i$ in region *i* after a total time $\Delta t$ occurred as follows:

$$\Delta N_i = \sum_j \frac{1}{l_{j,i}} N_{j,i} \Delta t - (1 - \rho_i) N_i \Delta t$$

$$\Delta M_i = \sum_j \frac{1}{l_{j,i}} M_{j,i} \Delta t - (1 - \rho_i) M_i \Delta t$$

where $N_{i,j}$ and $M_{i,j}$ represented the populations of normal and infected agents in the edge between regions *i* and *j* respectively. $N_{i,j}$ and $M_{i,j}$ were updated as follows:

$$\Delta N_{i,j} = (1-\rho_i)\frac{w_{ij}}{\sum_j w_{i,j}} N_i \Delta t - \frac{1}{l_{i,j}} N_{i,j} \Delta t$$

$$\Delta M_{i,j} = (1-\rho_i)\frac{w_{i,j}}{\sum_j w_{i,j}} M_i \Delta t - \frac{1}{l_{i,j}} M_{i,j} \Delta t$$

#### 6.3.6. Accrual of atrophy

Tissue loss was modeled as the result of two processes: the direct toxicity from the accumulation of infected agents in region *i* and the deafferentation occurring due to neuronal death in neighboring regions connected with region *i*. The atrophy accrual at time *t* within *Δt* in region *i* was given by:

$$\Delta L_i = k_1\left(1 - e^{-r_i(t)\Delta t}\right) + k_2 \sum_j \frac{w_{i,j}}{\sum_j w_{i,j}}\left(1 - e^{-r_j(t-1)\Delta t}\right)$$

where $r_i(t)$ represented the proportion of misfolded agents in region *i* at time *t*, $k_1$ was the weight (impact) of aSyn accumulation on modeling tissue loss, and $k_2$ was the weight (impact) of deafferentation from neighboring regions on tissue loss. Both $k_1$ and $k_2$ were set to 0.5 such that accumulation of infected agents and deafferentation had an equal effect on the growth of the atrophy simulated by the model.

### 6.4. Statistical analyses

#### *6.4.1. Longitudinal progression of atrophy*

To examine the progression of brain atrophy in PD patients, we performed linear mixed-effect modeling to investigate if the effect of time was significant over the regional deformation values at each time point, namely at baseline and after one, two, and four years of follow-up. This resulted in a set of 42 separate models, one for each brain region. The random intercept was assigned at the

patient level, while the fixed effect was the interaction of time with the age-and-sex corrected w-score DBM maps. The Benjamini-Hochberg procedure was used to control the false discovery rate (Benjamini et al., 2001) and a regional deformation change was considered significant when the *p*-value was below 0.05.

### *6.4.2. Fit between observed and modeled pathology*

The spread of aSyn was run for a total of 10,000 iterations after injecting pathology into the substantia nigra. The propagation speed v, which models the protein spreading rate, was set to 1. To check for robustness, variation in propagation speed (v) values ranging from 0.1 to 10 resulted in negligible difference on the model fit (Figure 6). The Model fit between simulated and observed atrophy was measured using Spearman's rank coefficient correlations. First, we investigated if the atrophy simulated in every region was significantly associated with the deformation value observed at baseline. At every time point (i.e., after one, two, and four years of follow-up), the regional simulated data was correlated with the regional observed atrophy difference, which is calculated by subtracting the baseline w-score DBM value from that of the follow-up time point. The peak fit between simulated and atrophy difference patterns observed between baseline and each time point corresponding to the highest correlation coefficient between the two metrics.

Next, we classified each region as either overestimated or underestimated based on the residual sign of the linear fit between empirical and simulated data. Overestimated regions tend to have less atrophy than what is predicted by the SIR model, while underestimated regions have more atrophy than what is simulated by the SIR model given the dynamics between connectivity and gene expression level. We explored the relationship between model estimation and regional

features such as network characteristics: node degree and node strength, in addition to SNCA and GBA level. Using the Brain Connectivity Toolbox (sites.google.com/site/bctnet) implemented in MATLAB, we calculated the node degree and strength for each region. Fundamentally, brain networks are composed of two basic components: nodes, distinct neural elements/regions, and edges, the pairwise connection between nodes, (Stanley et al., 2013). The node degree is the number of edges on a node in a binary network, while node strength quantifies the strength/weight of connectivity between pairs of nodes in a weighted network. Both are used to identify hubs, nodes with greater degree connectivity or centrality. The SNCA and GBA levels were determined from the AHBA atlas described earlier.

We also assessed the association of simulated data in every region to its assigned Braak stage using Spearman's rank coefficient correlations. For every PD group, the 42 regions were split into stages and each stage was correlated separately with the simulated data. The Braak hypothesis predicts that the progression of aSyn in PD occurs in a caudo-rostral fashion that can be described in six distinct stages. Regions in the revised DK-atlas used here ranges from Braak stage 3 to 6. We investigated if the regional simulated data predicted by the Agent-Based SIR Model reflect this hypothesis.

#### *6.4.3. Null models*

To investigate the impact of gene expression and the connectome's architecture on the pathology spread, we generated the peak fits between observed and simulated atrophy for every region in sets of 500 null models in which either one of these parameters was randomized. We then benchmarked the empirical peak fits to the average simulated peak fits obtained from the null models. For the

connectome null models, the impact of topology and/or geometry was investigated using rewired and repositioned null models. In rewired null networks, using the Maslov-Sneppen algorithm in the Brain Connectivity Toolbox (sites.google.com/site/bctnet), pairs of brain regions were randomly shuffled inside the structural matrix connectivity while preserving the network's original degree sequence and density; the rewiring per edge parameter was set to 100. In repositioned null networks, the spatial position of regions was randomly shuffled while preserving the network's original degree sequence and connection profile. In both cases, the shuffled matrix was inserted back into the model and used to generate a null peak fit between observed and simulated atrophy. For gene expression null models, each of *SNCA* and *GBA* regional expression values were shuffled separately. The empirical peak fit was then compared to the average of the simulated null peak fits using one-sample t-tests.

# 7. RESULTS

## *7.1. Participants*

A total of 1,068 T1-weighted scans, from 790 PD patients and 278 healthy controls, were obtained from the PPMI cohort. Of these, 199 scans were rejected: 193 failed quality control and 6 scans at PD year 3 and 5 were excluded due to the small sample size. This yields a total of 869 scans from 238 HC and 631 PD patients: 318 at baseline, 120 at one year, 108 at two years and 85 at four years. Only patients with a scan acquired at baseline and at least one follow-up time point were kept for further analysis, leaving samples of 113 patients between baseline and one year, 104 patients between baseline and two years, and 79 patients between baseline and four years. The 157 HC subjects at baseline were only selected for further statistical analysis due to the very small sample size of HC at follow-up years.

There were no significant age, sex, and education differences at baseline between patients and controls. However, PD patients had higher scores on the Geriatric Depression Scale ($p<0.001$) and lower scores on the following: Montreal Cognitive Assessment ($p<0.01$), the Symbol-Digit Modalities Test ($p<0.001$), and the Hopkins Verbal Learning Test-Revised ($p<0.01$). In PD patients, scores significantly worsened in comparison to baseline on the MDS-UPDRS-I, MDS-UPDRS-II, MDS-UPDRS-III, and the Scales for Outcomes in PD-Autonomic over the 4-year follow-up period ($p<0.01$). Also, phonemic fluency was significantly increased in patients between baseline and four years. Similarly, motor symptoms such as MDS-UPDRS III, II, and I, which are related to disease severity, have been shown to progress significantly in PD patients across the 4 years ($p < 0.001$) (Table 1).

### *7.2. Brain atrophy progresses over 4 years in PD*

Using linear mixed-effects models, 23 of the 42 brain regions showed significant deformation in PD over four years (Figure 1 and Table 2). Specifically, between baseline and year one, the progression was present in 14 regions, namely the putamen, caudate, middle temporal cortex, inferior temporal cortex, isthmus of the cingulate gyrus, precuneus, lateral occipital cortex, inferior parietal cortex, entorhinal cortex, banks of the superior temporal sulcus, parahippocampal gyrus, lingual and fusiform gyri, and lateral orbitofrontal cortex. Four additional regions became significantly deformed between baseline and year two, namely the rostral anterior cingulate cortex, supramarginal cortex, temporal pole, and insula. Unlike the other regions, the insula showed significant volume expansion at year 2, which is in line with the expansion of the sulcus due to perisylvian atrophy. After four years of follow-up, 5 other regions also became significantly

atrophied compared to baseline, namely the posterior cingulate cortex, superior parietal cortex, superior temporal cortex, accumbens area, and amygdala.

### *7.3. The agent-based SIR Model recreates atrophy progression*

Next, we used the agent-based SIR Model to simulate the spread of aSyn in the 42 regions and compared the simulated pattern of atrophy to the atrophy difference patterns observed between baseline and one year, two years, and four years of follow-up in PD. We found that the atrophy simulated by the model recreated the atrophy progression patterns observed at each time point (Figure 2). Specifically, the peak correlation between the simulated and observed atrophy at baseline was $r=0.58$ ($p<0.0001$) and occurred early during the simulated spread of aSyn ($500^{th}$ timestep). The peak correlation with the progression of atrophy between baseline and one year was $r=0.34$ ($p=0.03$, timestep 8533) at one year and $r=0.33$ ($p=0.03$, timestep 7182) at two years. In contrast, the simulated atrophy did not recreate the pattern of atrophy progression seen between baseline and four years, with the model underestimating atrophy overall. Given the network analysis on model estimation for every region, overestimated regions across all years appeared to have high node degree and strength in comparison to underestimated regions. Hence, overestimated regions had higher connections that would allow more misfolded aSyn to spread and eventually predicting more atrophy than what actually exists. We also found that overestimated regions tend to have less gene expression of SNCA and GBA overall across all years, which indicates that the SIR model may be augmenting the influence of connectivity over genetic expression for these regions Figure 3.

To Further evaluate how well the model's simulated data matches the empirical data across all the time points, cost function was measured for each of the 10,000 simulated time step. This was

quantified by calculating the Normalized Root Mean Square Error (NRMSE), which normalize the mean of observed data allowing for comparing model fits for different response variables (Otto et al., 2018): simulated atrophy based on quantification of asyn in region i, and empirical atrophy measure based on deformational changes. A drastic decrease in NRMSE was observed for all time points at early time steps (~$1000^{th}$), followed by slight increase of less than -0.7 for the rest of the spreading process. Overall, NRMSE supports the goodness of model fit to empirical data Figure 7.

To confirm these findings, we repeated the analyses with structural connectivity matrices containing instead 25%, 30%, and 40% of the most occurring edges. Results were highly similar (Table 3). Taken together, this demonstrates that the agent-based SIR Model recreates the progression of brain atrophy occurring over two years in PD and that other factors than the ones accounted for in our model may account for the atrophy observed after 4 years. Additionally, we investigated whether the simulated pattern of atrophy overlapped with the Braak staging scheme. Overall, all 4 Braak stages at BL were significantly correlated with the SIR simulated data ($stage3_{BL}: r = 0.54$, $stage4_{BL}: r = 0.52$, $stage5_{BL}: r = 0.69$, $stage6_{BL}: r = 0.91$). For year 1 and 2 of follow-up, only later Braak stages were significantly correlated ($stage3_{y1}: r = 0.14$, $stage4_{y1}: r = 0.3$, $stage5_{y1}: r = 0.5$, $stage6_{y1}: r = 0.54$; $stage3_{y2}: r = 0.02$, $stage4_{y2}: r = 0.22$, $stage5_{y2}: r = 0.37$, $stage6_{y2}: r = 0.32$) suggesting the disease severity later in the course of the disease after one year. This supports that the SIR model follows Braak staging hypothesis in recreating pathology of PD longitudinally (Figure 5).

### *7.4. The connectome's architecture shapes atrophy progression*

To investigate if the connectome's architecture was central to shaping the spread of aSyn pathology, we generated 500 rewired and repositioned null models in which the connectome topology and/or geometry were randomized. Using rewired models to shuffle the connectivity pattern between regions, we found that null correlations at the peak fit were always significantly lower than when using the real between-region connectivity profile ($r_{null}$ ~ 0.12, $p<0.0001$ at all time points; Figure 4), demonstrating that the progression of brain atrophy in PD is determined by how brain regions are connected with each other. Using repositioned models to shuffle the spatial embedding of brain regions, we also observed that the peak fit was significantly disrupted at baseline and the one- and two-year time points ($r_{null}$ ~0.29, $p<0.0001$ at all time points; Figure 4).

### *7.5. SNCA and GBA expression shapes atrophy progression*

To investigate the role of regional gene expression in how the spread of aSyn shapes the progression of atrophy over time, the local expression levels of *SNCA* or *GBA* region were separately randomized between brain regions. This systematically resulted in disrupted fits between the simulated and observed patterns of atrophy at baseline and during the following time points (*SNCA*: $r_{null}=0.33$ at baseline, $r_{null}=0.31$ at one year, and $r_{null}=0.31$ at two years with $p<0.0001$; *GBA*: $r_{null}=0.23$ at baseline, $r_{null}=0.09$ at one year, and $r_{null}=0.17$ at two years with $p<0.0001$; Figure 4). Altogether, these findings support that both the architecture of the connectome and the local expression of *SNCA* and *GBA* shape significantly the progression of brain atrophy in PD.

# 8. DISCUSSION

In this study, we evaluated the progression of atrophy in PD patients over 4 years and extended the use of the agent-based SIR Model in recapitulating the observed longitudinal spatiotemporal pattern of atrophy in PD patients to understand the underlying mechanism. Our findings showed three main insights: first, we found atrophy significantly progressed along four years of follow-up starting at caudate and putamen and spreading towards cortical regions. Second, the SIR model which introduces aSyn as an agent replicated *in silico* the pathology spread observed in PD patients longitudinally. Third, the SIR model demonstrated that cell-autonomous factors such as SNCA and GBA gene expression level, in addition to brain connectivity significantly contributed to shaping the spatiotemporal distribution of atrophy progression.

Investigating the evolution of brain atrophy in PD patients, we found that 50% ROIs showed atrophy progression in PD over 4 years. The regions with the strongest progression of atrophy over 4 years were the putamen and caudate, involved in motor and cognitive changes associated with PD, in addition to the middle and inferior temporal cortices. Atrophy in cortical regions such as the rostral anterior cingulate cortex and supramarginal cortex appeared after two years, whereas the posterior cingulate cortex and superior temporal cortex had atrophy only after year 4. This recapitulates other findings showing similar progression patterns such as ENIGMA study (Laansma et al., 2020). Interestingly, the substantia nigra, in which cell loss has been associated with the parkinsonian motor signs and symptoms leading to the clinical diagnosis of PD, was atrophied at baseline but did not show any atrophy progression during the follow-up years, suggesting that this region has already reached a floor effect, at least in terms of structural atrophy, at the time of clinical diagnosis. This finding provides a complementary insight into the

longitudinal posterior cortical pattern of brain atrophy presented recently by (Tremblay et al., 2021).

There are two theories of PD pathogenesis that may explain the mechanism underlying the observed pattern of atrophy: protein propagation and regional vulnerability (Brundin & Melki, 2017; Surmeier et al., 2017) . PD is characterized by the accumulation of misfolded aSyn in form of Lewy bodies. Several studies, especially in animal models, now support that aSyn pathology may spread in a prion-like fashion through brain networks. This has been postulated by the seminal model proposed by Braak, whereby the propagation would start inside the olfactory bulb or the enteric plexus and propagates ascendingly towards the midbrain and cortical areas (Braak et al., 2003). This has been supported by other post-mortem and neuroimaging investigations in humans. However, other evidence has also demonstrated that the brain's synaptic connectivity pattern does not completely explain the way by which aSyn pathology spread in the brain and that other cell-autonomous factors may explain some level of local selective vulnerability to the pathology spread. Indeed, some cell types appear more vulnerable to showing aSyn pathology, and aSyn expression levels may be one factor (Luna et al., 2018). Therefore, consistent with this, the higher the regional expression level of normal $\alpha$-synuclein agents, the greater the likelihood of region vulnerability to the accumulation of misfolded proteins. These two theories were incorporated into the dynamic SIR model to recreate and understand the atrophy progression pattern.

Next, we used an agent-based framework to simulate *in silico* the spread of aSyn considering information from gene expression and connectivity simultaneously. Then, we compared the simulated pattern to the deformation-based tissue atrophy progression patterns observed in a large

cohort of *de novo* PD patients followed over 1, 2, and 4 years. Previous computational models that simulated the spread of aSyn mostly relied on a connectivity-based diffusion mechanism (Pandya et al., 2019) that may have overlooked the importance of cell-autonomous factors in shaping the progression of atrophy in PD or other neurodegenerative diseases (Weickenmeier et al., 2018). The advantage of the agent-based SIR model is to integrate several non-cell-autonomous and cell-autonomous factors all at once to test humans' hypotheses related to the prion-like spread of pathology and the selective vulnerability to pathology. This model has been shown to accurately recreate the atrophy pattern observed at baseline in *de novo* PD patients (Zheng et al., 2019), but the ability of the model to predict the progression of atrophy remains unknown. In this study, we show that the simulated atrophy pattern generated by the agent-based SIR model significantly recreates the tissue deformational changes observed in PD over one and two years. More specifically, the model, particularly at the earlier time steps, replicated the atrophy found at baseline in early PD patients, with a peak at around (T= 400). The model fit drops at later timesteps because simulated data predicts more atrophy than found at baseline, consistent with (Zheng et al., 2019) findings when DBM was calculated using FSL. At one and two years of follow-up, the peak fit was found at later time steps during the spreading process (T=~3000). In contrast, the model did not recreate the atrophy difference observed after 4 years. One reason for this may be due to underestimation of the model to atrophy observed at year4. The underestimated regions by the model were found to have low degree node and strength, hence fewer connections for the agent to spread. Another possibility is that the smaller sample size of PD patients who were available for a 4-year MRI acquisition in addition to other factors that might affect the model such as incremental cell loss during the spreading process.

The regional aSyn concentration was modulated in the SIR model to assess regions' vulnerability to pathology accumulation. Shuffling the expression level of either SNCA or GBA resulted in significantly disrupted fit between observed and simulated data across all time points, suggesting the importance of genetic expression of both genes in shaping the spatial pattern of disease spread longitudinally. In other words, the regional transcription profiles of SNCA and GBA, which influence the asyn concentration: synthesis and clearance respectively, contribute to PD atrophy progression pattern. In line with other studies, GBA mutation which is responsible for autosomal recessive disorders turned out to be the most common genetic risk of PD (Riboldi & Di Fonzo, 2019) ; SNCA variants and mutations are also found to be risk factors for PD and contribute to the pathogenesis of the disease (Aharon-Peretz et al., 2004; Campêlo & Silva, 2017). Similarly, the randomization of the connectome topology (rewired null models) and the spatial positions of regions (spatial null models) resulted in a disrupted fit between observed and simulated data, supporting the significant role of the brain's connectivity pattern and geometric topology in shaping disease progression across all years. Consistent with other findings in animal studies, the neuronal spread of asyn follows a prion-like cascade that underlies the spatiotemporal distribution of Lewy bodies (Luk et al., 2012).

Although the agent-based SIR model recreated the spatiotemporal distribution of atrophy in PD over time, there are a few study limitations to be mentioned. First, PPMI dataset might not be reflective of the general PD population as it is based on recruiting younger and less cognitively patients at baseline. However, it is the largest longitudinal dataset of PD with imaging, genetics, clinical and demographic data. Second, the model did not account for other factors that may be relevant to the spread in general such as incremental cell loss or the impact of gene expression on

cellular dynamics such as the protein folding, post-translational modification, and subcellular localization (Miraglia et al., 2018). It is worth considering that adding features increases the complexity of the model and can lead to overfitting especially with small sample size datasets (Kaul and Ventikos, 2015). One of the future directions is to extend the application of the SIR model to predict disease trajectory in other groups/datasets related to PD or syncleiopathies in general.

In conclusion, this study shows regional deformational changes in PD longitudinally. Subcortical atrophy affecting caudate and striatium are found to progress early while cortical regions seem to progress later at year 2 of follow-up and above. The mechanism behind these changes over 4 years, which was investigated using the SIR model, is dependent on connectivity and geometric topology of brain network in addition to SNCA and GBA genetic expression level. The SNCA and GBA are used in the model to set the concentration of asyn, which implies that asyn expression and connectivity shape atrophy progression. This further demonstrates that the agent-based SIR model is a promising tool for testing hypotheses regarding the mechanical underpinnings of aSyn spread in the human brain.

# 9. List of Tables & Figures

**Figure1: Regional deformational changes in PD over 4 years**

**(A)**

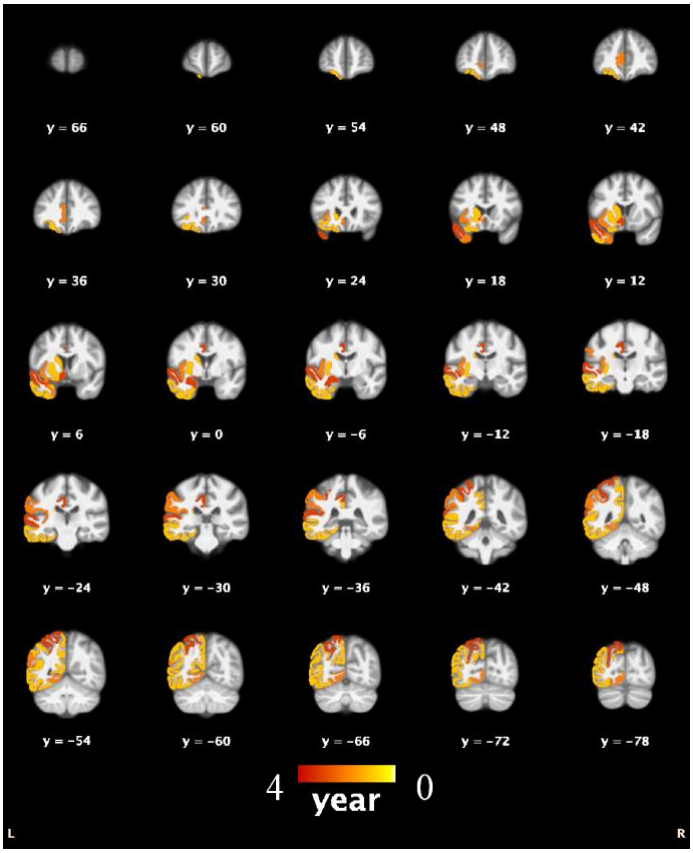


**(B)**

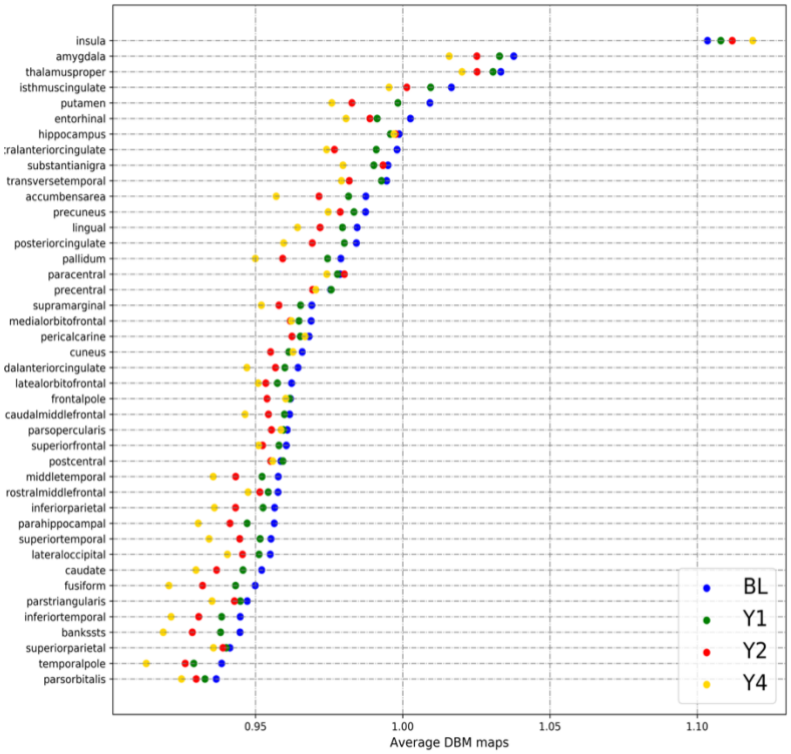


**Figure 1. Regional Longitudinal changes in PD over 4 years. (A)** Brain maps showing the regions that were significantly deformed at each time point compared to baseline. Only the left hemisphere is shown due to limitations regarding the gene expression scores and the structural connectivity measures. **(B)** The dot chart represents DBM maps observed at baseline and during follow-up time points (i.e., one, two, and four years) in patients with PD for the 42 regions.

**Figure2: SIR model fit with observed data**

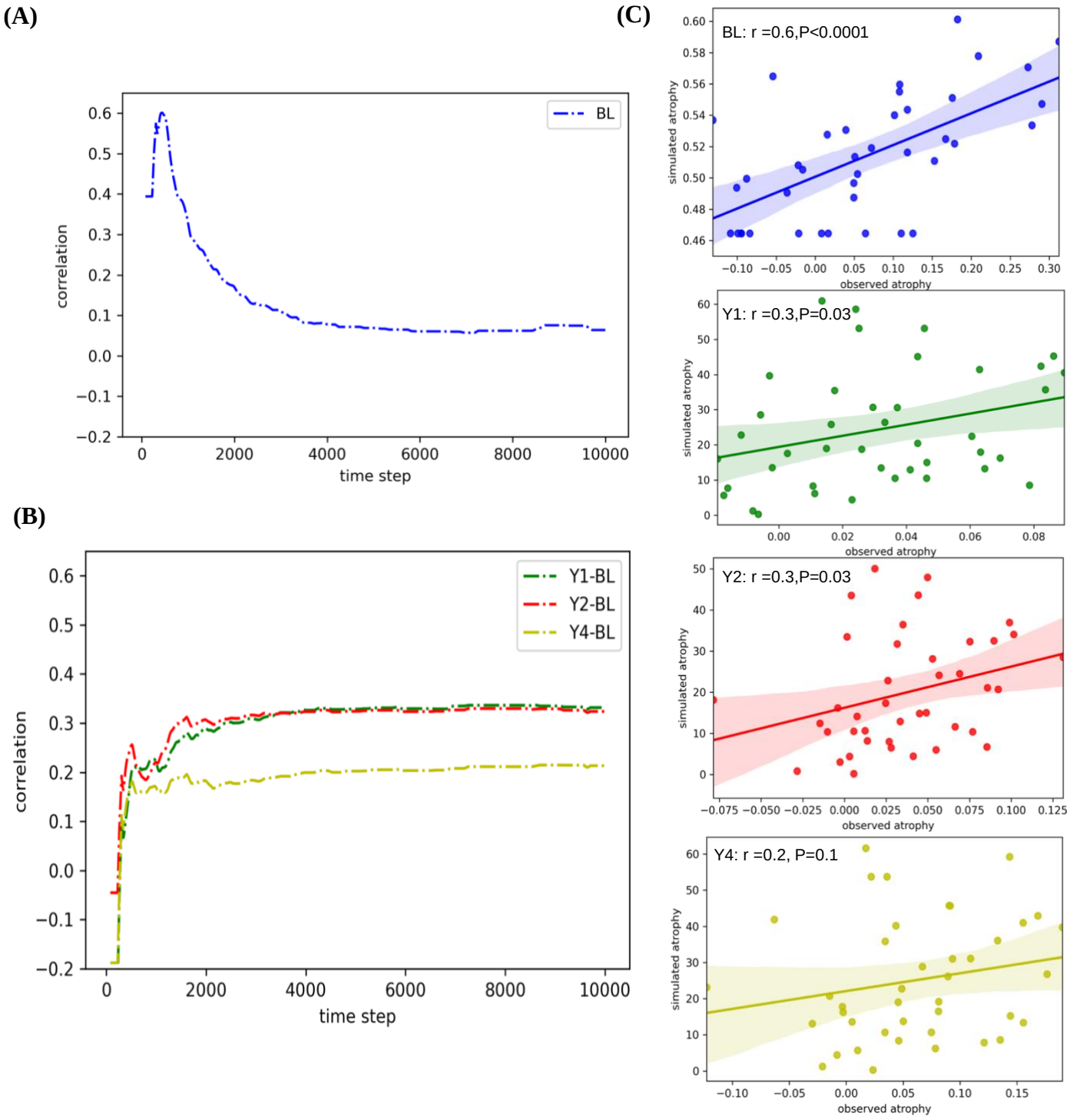


**Figure 2: The agent-based SIR Model recreates the progression of brain atrophy. (A)** The peak fit was assessed using Spearman's rank correlation coefficient at each of the 10,000 simulation timestep between simulated pattern of atrophy to the patterns of atrophy observed at

baseline and **(B)** atrophy difference at each follow-up time point (i.e., one, two, and four years). **(C)** Scatterplots showing the observed and simulated atrophy for each region at each simulation peak correlation fit.

**Figure3: Model's regional estimation**

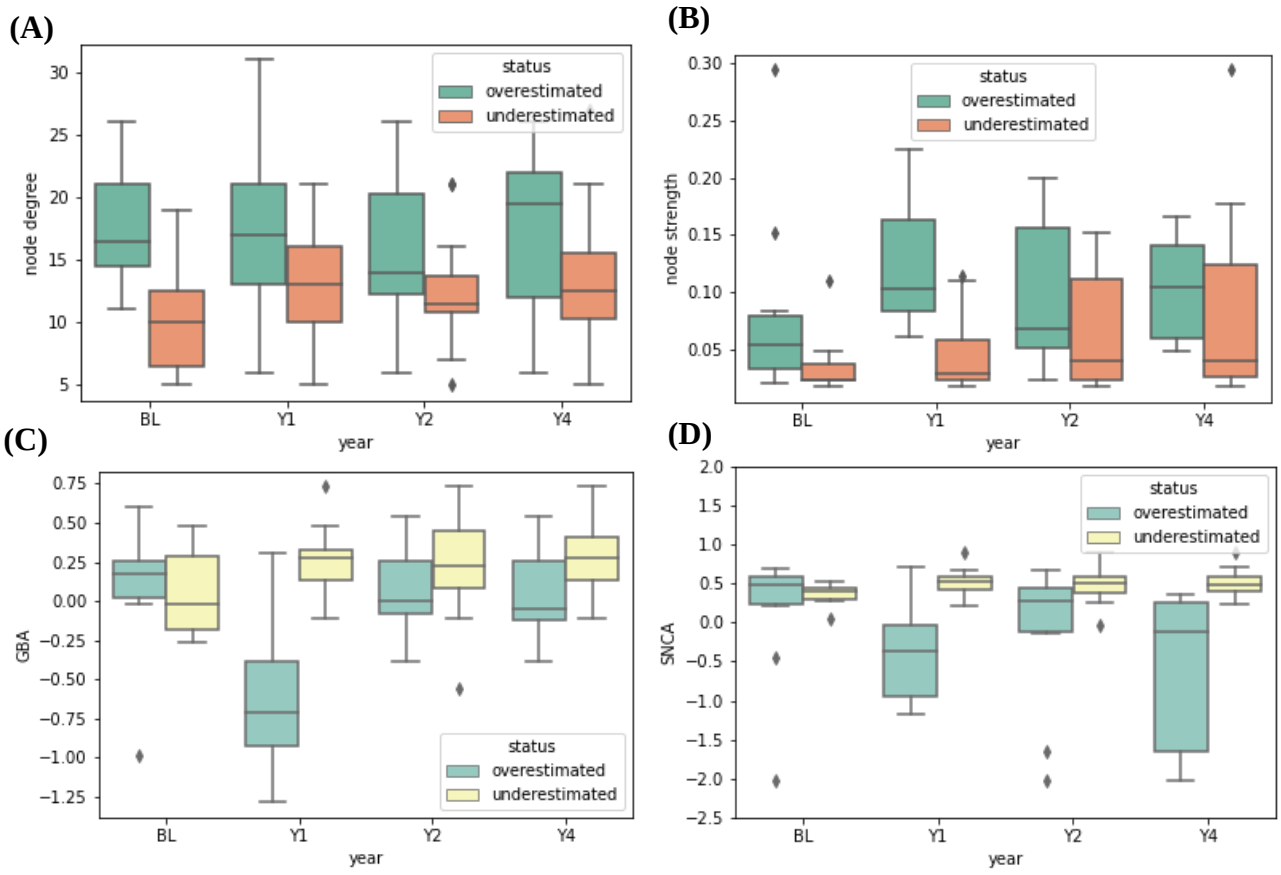


**Figure 3: Model features of overestimated and underestimated regions.** Regions were classified based on the residual sign of the linear fit between observed and simulated data (**A)** node degree **(B)** node strength **(C)** SNCA z-score expression level **(D)** GBA z-score expression level of overestimated vs. underestimated regions for each time point (Bl, 1, 2, 4 years of follow-up).

**Figure4: Null models**

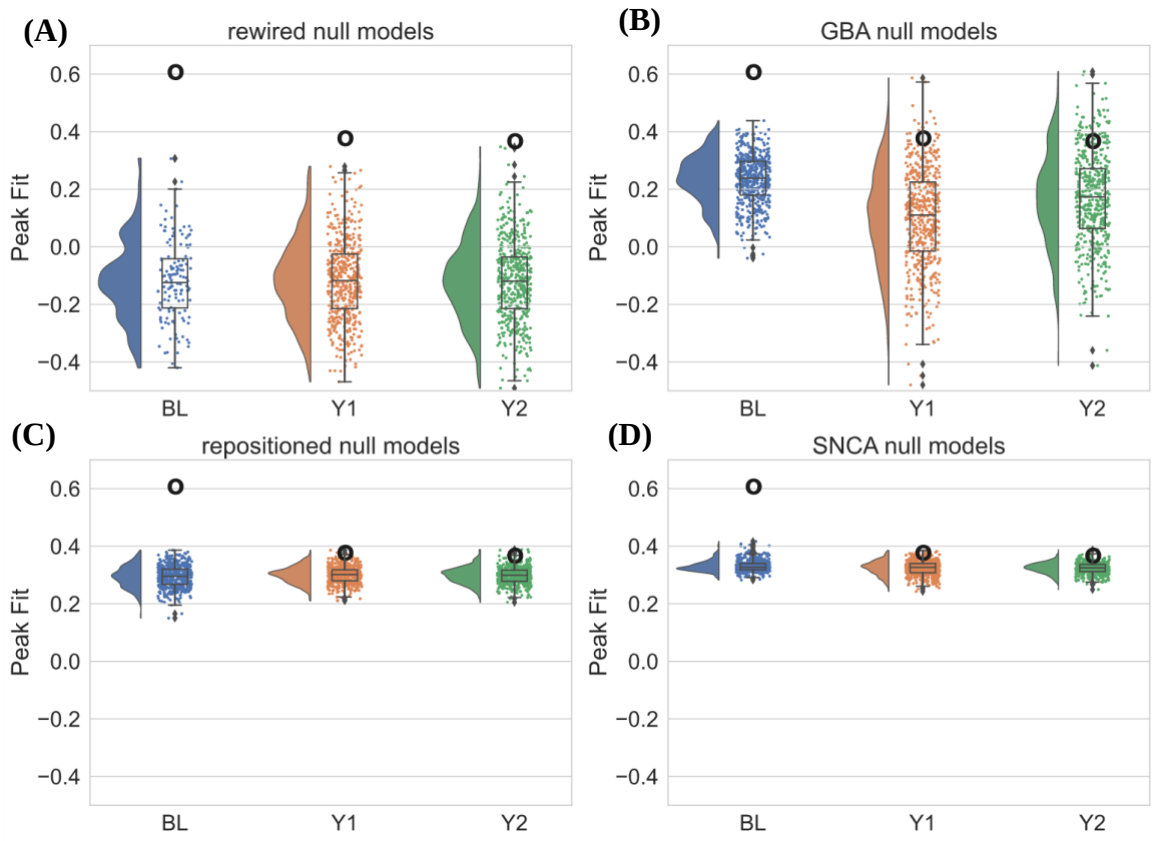


**Figure 4. The architecture of the connectome and the local expression of *SNCA* and *GBA* shape brain atrophy progression in PD.** the distribution of null peak correlation fits generated when shuffling randomly the **(A)** connectivity weights between regions, **(B)** the local expression of *GBA*, **(C)** the spatial embedding of regions, or **(D)** the local expression of *SNCA* compared to when the peak fit is generated using the original parameter. The comparisons are made at baseline and for the one- and two-year time points. The black circle refers to the value of the peak correlation fit between the observed pattern of atrophy and the simulated pattern with the original non-shuffled parameter. All null models represent a significant difference between the original fit and the shuffled fits at $p<0.0001$ using one-tailed t test.

**Figure5: SIR model overlaps with the Braak staging scheme**

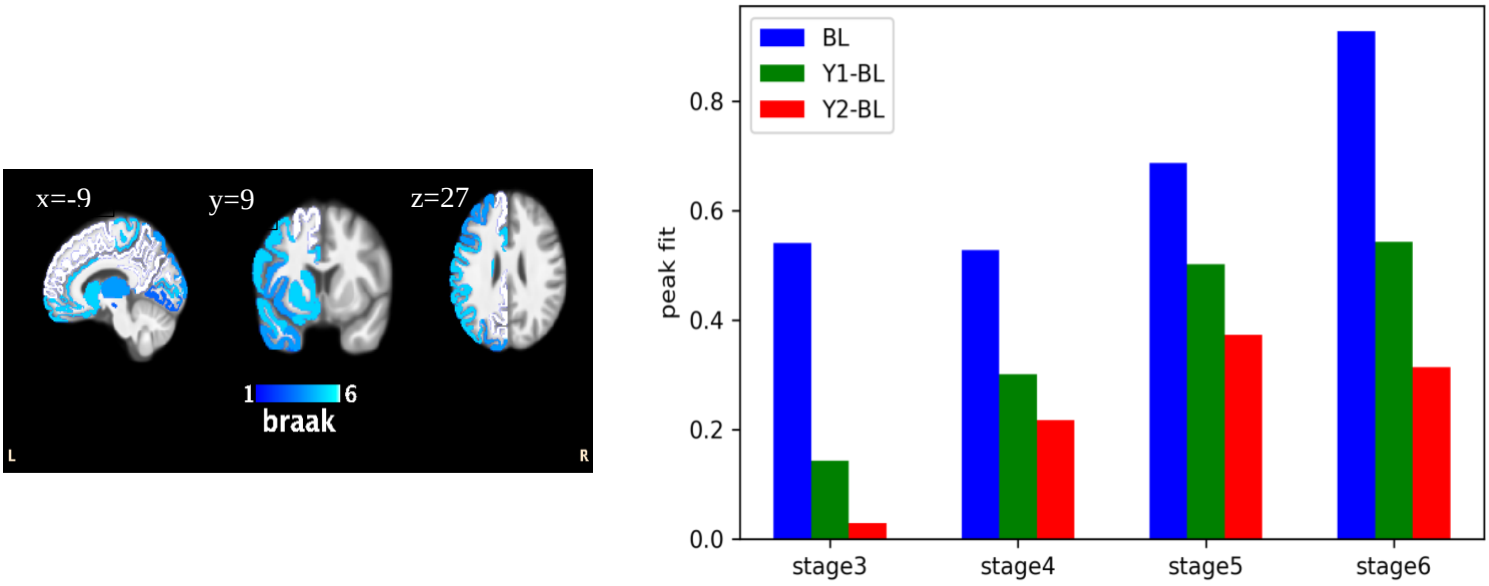


**Figure 5. The SIR model replicates the development of parkinson's pathology following braak staging hypothesis. (A)** braak staging map for each of the 42 ROIs in the DK-revised atlas used in this study. **(B)** Peak fit between simulated and atrophy patterns at each time point(BL, 1, 2 years of follow-up) at each braak stage. Peak fit is the highest Spearmen's rank correlation between simulated and empirical measures.

**Figure6: Model robustness to changes in free parameters**

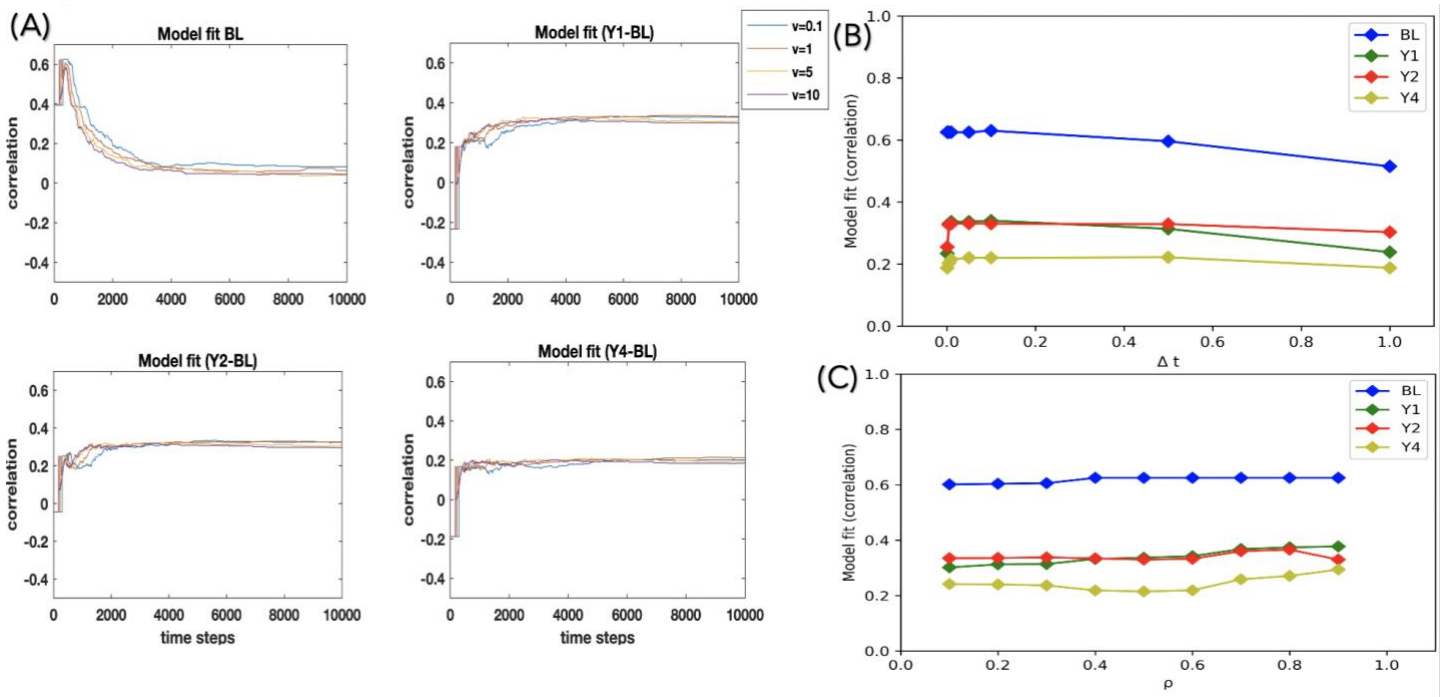


**Figure 6. Testing model robustness to changes in free parameters.** The model fit measured using Spearman's rank correlation coefficients is robust to variations in **(A)** the propagation speed (v), tested using values ranging from 0.1 to 10 (v=1 in the main text), **(B)** the timestep increment ($\Delta t$), tested using values ranging from 0.001 to 1 ($\Delta t = 0.01$ in the main text), and **(C)** the probability of an agent staying in region $i$ ($\rho$), tested using values ranging from 0.1 to 0.9 ($\rho$ = 0.5 in the main text) at the connection density of 35% used for main results. All parameters were tested at each time point, with distinct lines indicating peak correlation fits at baseline, at baseline versus one year, at baseline versus two years, and at baseline versus four years of follow-up.

**Figure7:** Cost function assessing SIR model performance

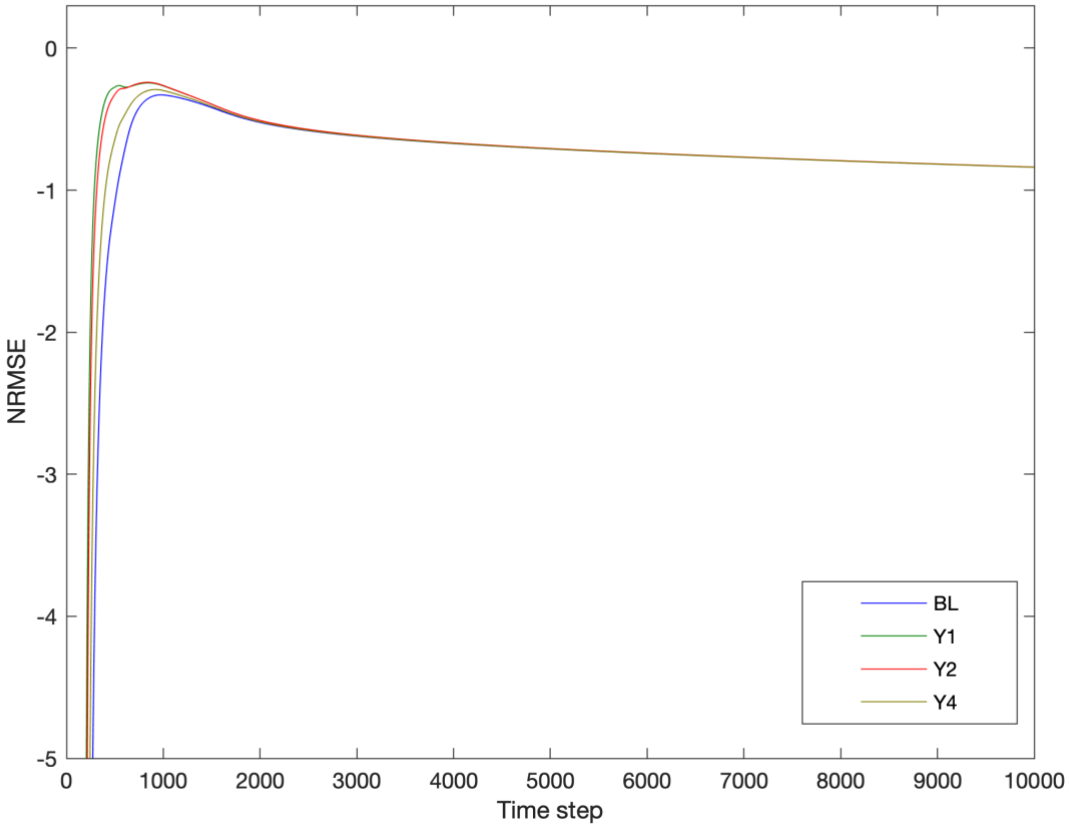


**Figure 7:** Cost function of the model fit between simulated and empirical atrophy was assessed using Normalized Root Mean Squared Error (NRMSE). NRMSE was calculated across all the 10,000 simulated time steps for every time point (BL: baseline, Y1: difference in atrophy at year1, Y2: difference in atrophy at year2, Y4: difference in atrophy at year4).

**Table1:** The demographics and clinical characteristics of participants

| **Variables** | **Baseline** | | | **1-year follow up** | | **2-year follow-up** | | **4-year follow-up** | |
|---|---|---|---|---|---|---|---|---|---|
| | **PD** | **HC** | ***p*** | **PD** | ***p*** | **PD** | ***p*** | **PD** | ***p*** |
| Sample size | 318 | 157 | | 120 | | 108 | | 85 | |
| Age | 60.9 (10.0) | 60.1 (11.9) | 0.41[a] | 60.9 (10.7) | 0.98[a] | 62.6 (9.3) | 0.13[a] | 64.4 (9.9) | **0.005**[a] |
| Sex (% male) | 201 (63%) | 103 (66%) | 0.68[b] | 75 (63%) | 0.98[b] | 68 (63%) | 0.94[b] | 58 (69%) | 0.46[b] |
| Education, years | 15.77 (2.94) | 16.06 (2.94) | 0.31[a] | 15.20 (2.93) | 0.07[a] | 15.14 (2.66) | 0.05[a] | 15.36 (2.75) | 0.2[a] |
| MDS-UPDRS-III | 18.52 (7.82) | 1.14 (2.19) | **<0.001**[a] | 21.63 (10.48) | **0.001**[a] | 23.33 (11.80) | **<0.001**[a] | 23.6 (10.1) | **<0.001**[a] |
| MDS-UPDRS-II | 5.20 (4.06) | 0.41 (0.97) | **<0.001**[c] | 7.14 (4.71) | **<0.001**[c] | 7.29 (4.94) | **<0.001**[c] | 9.03 (5.66) | **<0.001**[c] |
| MDS-UPDRS-I | 3.51 (2.70) | 2.44 (2.64) | **<0.001**[c] | 4.84 (2.42) | **<0.001**[c] | 4.97 (3.13) | **<0.001**[c] | 6.35 (3.89) | **<0.001**[c] |
| GDS | 2.27 (2.40) | 1.13 (2.24) | **<0.001**[c] | 2.53 (2.82) | 0.11[c] | 2.39 (2.68) | 0.32[c] | 2.3 (2.2) | 0.46[c] |
| STAI | 93.52 (7.90) | 94.31 (7.14) | 0.29[a] | 91.85 (7.70) | 0.053[a] | 92.10 (7.21) | 0.10[a] | 92.51 (7.75) | 0.29 |

| | | | | | | | | | |
|---|---|---|---|---|---|---|---|---|---|
| SCOPA-AUT | 9.27 (5.94) | 3.78 (3.92) | **<0.001**[c] | 10.27 (2.19) | **0.02**[c] | 10.77 (5.53) | **<0.001**[c] | 12.23 (6.25) | **<0.001**[c] |
| Probable RBD, % cases | 120 (38%) | 33 (21%) | **<0.001**[b] | 35 (29%) | **0.008**[b] | 38 (35%) | 0.08[b] | 36 (42%) | 0.6[b] |
| MoCA | 27.4 (2.1) | 28.3 (1.1) | **<0.001**[c] | 27.0(0.9) | 0.29[c] | 27.0 (2.4) | 0.12[c] | 27.5 (2.6) | 0.10[c] |
| SDMT | 41.52 (9.34) | 46.9 (11.1) | **<0.001**[a] | 41.22 (10.7) | 0.77[a] | 40.96 (10.03) | 0.59[a] | 40.2 (10.9) | 0.27[a] |
| LNS | 10.73 (2.72) | 10.93 (2.64) | 0.46[a] | 10.63 (2.68) | 0.73[a] | 10.73 (2.78) | 0.9[a] | 10.55 (3.19) | 0.6[a] |
| BJLO | 25.68 (4.18) | 26.36 (3.75) | 0.06[c] | 25.15 (4.45) | 0.12[c] | 25.70 (4.07) | 0.47[c] | 26.29 (3.54) | 0.29[c] |
| Semantic fluency | 14.52 (4.59) | 14.96 (4.15) | 0.12[c] | 14.28 (4.14) | 0.13[c] | 14.64 (4.15) | 0.47[c] | 14.16 (4.66) | 0.21[c] |
| Phonemic fluency | 13.27 (4.73) | 14.04 (4.45) | 0.09[a] | 13.71 (4.56) | 0.4[a] | 13.98 (4.62) | 0.18[a] | 14.75 (4.59) | **0.01**[a] |
| HVLT-R, total recall | 24.8 (5.0) | 26.0 (4.5) | **0.01**[a] | 24.5 (5.6) | 0.6[a] | 24.3 (5.7) | 0.4[a] | 24.8 (5.8) | 0.9[a] |

| | | | | | | | | | |
|---|---|---|---|---|---|---|---|---|---|
| HVLT-R, delayed recall | 8.57 (2.48) | 9.27 (2.26) | **0.002** [c] | 8.50 (2.76) | 0.5 [c] | 8.50 (2.97) | 0.4 [c] | 8.49 (3.12) | 0.3 [c] |
| HVLT-R, recognition | 11.24 (1.19) | 11.51 (0.82) | **0.006** [c] | 11.24 (1.48) | 0.2 [c] | 11.35 (1.71) | **0.006** [c] | 11.31 (0.90) | 0.5 [c] |

**Table 1: Demographic and clinical characteristics of patients up to 4 years of follow-up included from the Parkinson's Progression Markers Initiative.** Data are shown as mean (standard deviation). P-value of followup year is calculated in respect to baseline of PD using: [a] student t-test, [b] chi-square test, [c] Mann-Whitney U test.

BJLO = Benton Judgment of Line Orientation; GDS = Geriatric Depression Scale; HC = healthy controls; HVLT-R = Hopkins Verbal Learning Test-Revised; LNS = Letter-Number Sequencing; MDS-UPDRS = Movement Disorders Society-Unified Parkinson's Disease Rating Scale; MoCA = Montreal Cognitive Assessment; PD = Parkinson's disease; RBD = REM sleep behavior disorder; SCOPA-AUT = Scales for Outcomes in Parkinson's Disease-Autonomic; SDMT = Symbol-Digit Modalities Test; STAI = State-Trait Anxiety Inventory.

**Table2: Result of Linear mixed effects models**

| Regions | Year 1 | | | Year 2 | | | Year 4 | | |
|---|---|---|---|---|---|---|---|---|---|
| | **Coeff, SE** | **p** | **95% CI** | **Coeff, SE** | **p** | **95% CI** | **Coeff, SE** | **p** | **95% CI** |
| Lateral orbitofrontal | -0.052, 0.023 | 0.049 | [-0.096 -0.008] | -0.073, 0.023 | 0.006 | [-0.119 -0.028] | -0.103, 0.026 | 0.00036 | [-0.154 -0.053] |
| Pars orbitalis | -0.035, 0.021 | 0.17 | [-0.076 0.006] | -0.031, 0.021 | 0.24 | [-0.073 0.011] | -0.048, 0.024 | 0.087 | [-0.094 -0.002] |
| Frontal pole | 0.014, 0.034 | 0.76 | [-0.052 0.081] | -0.051, 0.035 | 0.24 | [-0.120 0.018] | -0.039, 0.039 | 0.43 | [-0.115 0.037] |
| Medial orbitofrontal | -0.019, 0.021 | 0.47 | [-0.06 0.022] | -0.024, 0.021 | 0.37 | [-0.066 0.018] | -0.049, 0.024 | 0.081 | [-0.095 -0.003] |
| Pars triangularis | 0.002, 0.017 | 0.94 | [-0.031 0.035] | 0.026, 0.017 | 0.22 | [-0.008 0.06] | 0.016, 0.019 | 0.52 | [-0.022 0.053] |
| Pars opercularis | 0.011, 0.013 | 0.52 | [-0.015 0.037] | 0.013, 0.014 | 0.44 | [-0.014 0.04] | 0.026, 0.015 | 0.17 | [-0.004 0.055] |
| Rostral middle frontal | -0.037, 0.022 | 0.19 | [-0.08 0.007] | -0.022, 0.023 | 0.44 | [-0.067 0.023] | -0.046, 0.025 | 0.14 | [-0.095 0.004] |

| | | | | | | | | | |
|---|---|---|---|---|---|---|---|---|---|
| Superior frontal | -0.008, 0.018 | 0.76 | [-0.043 0.027] | 0.00, 0.018 | 0.99 | [-0.036 0.036] | -0.028, 0.02 | 0.26 | [-0.068 0.011] |
| Caudal middle frontal | 0.009, 0.014 | 0.63 | [-0.018 0.036] | -0.002, 0.014 | 0.94 | [-0.029 0.026] | -0.009, 0.016 | 0.69 | [-0.039 0.022] |
| Precentral | 0.017, 0.016 | 0.43 | [-0.016 0.049] | -0.002, 0.017 | 0.94 | [-0.035 0.032] | 0.004, 0.019 | 0.89 | [-0.032 0.041] |
| Paracentral | 0.001, 0.014 | 0.94 | [-0.025 0.028] | -0.006, 0.014 | 0.76 | [-0.034 0.22] | -0.02, 0.016 | 0.30 | [-0.051 0.01] |
| Rostral anterior cingulate | -0.03, 0.015 | 0.103 | [-0.059 0] | -0.036, 0.016 | 0.048 | [-0.067 -0.006] | -0.075, 0.017 | 0.00011 | [-0.109 -0.042] |
| Caudal anterior cingulate | -0.012, 0.01 | 0.33 | [-0.032 0.008] | 0.00, 0.01 | 0.98 | [-0.02 0.021] | 0.006, 0.12 | 0.703 | [-0.017 0.029] |
| Posterior cingulate | -0.017, 0.017 | 0.44 | [-0.051 0.017] | -0.019, 0.018 | 0.410 | [-0.054 0.016] | -0.054, 0.02 | 0.017 | [-0.093 -0.016] |
| Isthmus of cingulate | -0.057, 0.016 | 0.001 | [-0.088 -0.025] | -0.051, 0.017 | 0.0075 | [-0.083 -0.018] | -0.119, 0.018 | <0.0001 | [-0.155 -0.083] |
| Postcentral | 0.013, 0.016 | 0.53 | [-0.019 0.045] | -0.009, 0.017 | 0.70 | [-0.042 0.024] | -0.036, 0.019 | 0.109 | [-0.073 0.001] |

| | | | | | | | | | |
|---|---|---|---|---|---|---|---|---|---|
| Supramarginal | -0.035, 0.017 | 0.080 | [-0.067 -0.002] | -0.044, 0.017 | 0.029 | [-0.077 -0.01] | -0.077, 0.019 | 0.00032 | [-0.114 -0.04] |
| Superior parietal | -0.20, 0.016 | 0.33 | [-0.052 0.012] | -0.027, 0.017 | 0.19 | [-0.061 0.006] | -0.72, 0.019 | 0.0007 | [-0.109 -0.035] |
| Inferior parietal | -0.049, 0.017 | 0.010 | [-0.082 -0.016] | -0.065, 0.017 | 0.00087 | [-0.098 -0.031] | -0.142, 0.019 | <0.0001 | [-0.18 -0.105] |
| Precuneus | -0.047, 0.014 | 0.002 | [-0.074 -0.021] | -0.047, 0.014 | 0.0028 | [-0.075 -0.02] | -0.134, 0.015 | <0.0001 | [-0.164 -0.103] |
| Cuneus | -0.022, 0.013 | 0.163 | [-0.083 0.151] | -0.013, 0.013 | 0.440 | [-0.046 0.013] | -0.022, 0.014 | 0.202 | [-0.051 0.006] |
| Pericalcarine | -0.012, 0.017 | 0.59 | [-0.047 0.022] | 0.007, 0.018 | 0.79 | [-0.029 0.042] | 0.022, 0.02 | 0.39 | [-0.017 0.061] |
| Lateral occipital | -0.044, 0.014 | 0.007 | [-0.071 -0.016] | 0.015 | 0.021 | [-0.067 -0.01] | 0.016 | <0.0001 | [-0.126 -0.063] |
| Lingual | -0.036, 0.015 | 0.042 | [-0.066 - 0.006] | -0.030, 0.016 | 0.11 | [-0.061 0.001] | -0.085, 0.017 | <0.0001 | [-0.119 -0.051] |
| Fusiform | -0.06, 0.022 | 0.018 | [-0.104 -0.017] | -0.083, 0.023 | 0.0013 | [-0.128 -0.038] | -0.179, 0.025 | <0.0001 | [-0.229 -0.130] |
| Parahippocampal | -0.077, 0.029 | 0.02 | [-0.133 -0.02] | -0.089, 0.03 | 0.0084 | [-0.147 -0.031] | -0.159, 0.33 | <0.0001 | [-0.223 -0.095] |

| | | | | | | | | | |
|---|---|---|---|---|---|---|---|---|---|
| Entorhinal | -0.074, 0.025 | 0.011 | [-0.124 - 0.024] | -0.108, 0.026 | 0.00032 | [-0.159 -0.056] | -0.120, 0.029 | <0.0001 | [-0.177 -0.063] |
| Temporal pole | -0.068, 0.03 | 0.051 | [-0.126 -0.01] | -0.073, 0.031 | 0.043 | [-0.133 -0.013] | -0.130, 0.034 | 0.0007 | [-0.196 -0.064] |
| Inferior temporal | -0.074, 0.02 | 0.001 | [-0.113 -0.036] | -0.065, 0.02 | 0.0051 | [-0.105 -0.025] | -0.168, 0.022 | <0.0001 | [-0.212 -0.124] |
| Middle temporal | -0.065, 0.017 | 0.001 | [-0.099 - 0.031] | -0.081, 0.018 | <0.0001 | [-0.116 -0.046] | -0.179, 0.02 | <0.0001 | [-0.218 -0.141 |
| Banks of superior temporal sulcus | -0.031, 0.012 | 0.018 | [-0.054 - 0.009] | -0.039, 0.012 | 0.0037 | [-0.063 -0.016] | -0.041, 0.013 | 0.0057 | [-0.067 -0.016] |
| Superior temporal | -0.027, 0.017 | 0.19 | [-0.06 0.006] | -0.026, 0.017 | 0.22 | [-0.06 0.008] | -0.065, 0.019 | 0.0026 | [-0.102 -0.028] |
| Transverse temporal | 0.009, 0.009 | 0.44 | [-0.009 0.027] | 0.013, 0.009 | 0.29 | [-0.006 0.031] | 0.007, 0.01 | 0.64 | [-0.014 0.027] |
| Insula | 0.039, 0.027 | 0.25 | [-0.041 0.092] | 0.077, 0.028 | 0.018 | [0.022 0.132] | 0.116, 0.031 | <0.0001 | [0.056 0.177] |
| Thalamus | 0.010, 0.023 | 0.76 | [-0.036 0.056] | 0.009, 0.024 | 0.80 | [-0.039 0.056] | 0.060, 0.027 | 0.057 | [0.007 0.112] |
| Caudate | -0.061, 0.017 | 0.002 | [-0.095 -0.027] | -0.095, 0.018 | <0.0001 | [-0.131 - 0.06] | -0.097, 0.02 | <0.0001 | [-0.136 -0.058] |

| | | | | | | | | | |
|---|---|---|---|---|---|---|---|---|---|
| Putamen | -0.089, 0.021 | 0.001 | [-0.131 - 0.048] | -0.089, 0.022 | 0.00032 | [-0.132 -0.046] | -0.092, 0.024 | 0.0008 | [-0.139 -0.044] |
| Pallidum | -0.004, 0.029 | 0.94 | [-0.06 0.052] | -0.039, 0.03 | 0.29 | [-0.098 0.019] | 0.003, 0.033 | 0.95 | [-0.061 0.067] |
| Accumbens | -0.036, 0.029 | 0.32 | [-0.093 0.021] | -0.066, 0.03 | 0.06 | [-0.125 -0.007] | -0.104, 0.033 | 0.0058 | [-0.169 -0.039] |
| Hippocampus | -0.038, 0.023 | 0.18 | [-0.084 0.008] | -0.004, 0.024 | 0.93 | [-0.052 0.043] | -0.032, 0.027 | 0.34 | [-0.084 0.020] |
| Amygdala | -0.006, 0.034 | 0.93 | [-0.072 0.06] | -0.057, 0.035 | 0.19 | [-0.125 0.012] | -0.161, 0.038 | 0.0002 | [-0.236 -0.086] |
| Substantia Nigra | 0.005, 0.35 | 0.94 | [-0.064 0.073] | 0.045, 0.036 | 0.33 | [-0.026 0.116] | -0.024, 0.04 | 0.66 | [-0.101 0.054] |

**Table 2. Progression of brain atrophy in PD.** Results of the 42 linear mixed effect models showing progression of each region at year 1,2, and 4 of follow-up in comparison to baseline. The significance threshold reported here is presented after FDR correction for multiple comparisons. Coeff = coefficient; FDR = false discovery rate; SE = standard error; CI = 95 % confidence interval.

**Table3: Testing model fit aganist different network density**

| Time point | **40% density** | | | **35% density** | | | **30% density** | | |
|---|---|---|---|---|---|---|---|---|---|
| | **r** | **timestep** | **P-value** | **r** | **timestep** | **P-value** | **r** | **timestep** | **P-value** |
| BL | 0.58 | 457 | $6.39e^{-5}$ | 0.58 | 500 | $1.24e^{-5}$ | 0.53 | 260 | $3.2e^{-4}$ |
| BL versus Y1 | 0.31 | 6417 | 0.04 | 0.34 | 8533 | 0.03 | 0.33 | 9354 | 0.03 |
| BL versus Y2 | 0.31 | 6417 | 0.04 | 0.33 | 7182 | 0.03 | 0.33 | 3252 | 0.03 |

**Table 3. The findings remain similar when using different network densities.** The peak Spearman's correlations between the simulated pattern of atrophy and the patterns of atrophy observed at baseline and at the one- and two-year time points remain insignificantly similar when simulating the spread using network densities representing the 30%, 35%, and 40% of the strongest connections of the structural connectivity matrix.

# 9. REFERENCES

Hughes, A. J., Daniel, S. E., Kilford, L., & Lees, A. J. (1992). Accuracy of clinical diagnosis of idiopathic Parkinson's disease: a clinico-pathological study of 100 cases. Journal of neurology, neurosurgery & psychiatry, 55(3), 181-184.

Postuma, R. B., Berg, D., Stern, M., Poewe, W., Olanow, C. W., Oertel, W., ... & Deuschl, G. (2015). MDS clinical diagnostic criteria for Parkinson's disease. Movement disorders, 30(12), 1591-1601.

Poewe, W., Seppi, K., Tanner, C. M., Halliday, G. M., Brundin, P., Volkmann, J., ... & Lang, A. E. (2017). Parkinson disease. Nature reviews Disease primers, 3(1), 1-21

Benjamini, Y., Drai, D., Elmer, G., Kafkafi, N., and Golani, I. (2001). Controlling the false discovery rate in behavior genetics research. Behav Brain Res 125, 279-284.

Braak, H., Del Tredici, K., Rub, U., de Vos, R.A., Jansen Steur, E.N., and Braak, E. (2003). Staging of brain pathology related to sporadic Parkinson's disease. Neurobiol Aging 24, 197-211.

Braak, H., Ghebremedhin, E., Rub, U., Bratzke, H., and Del Tredici, K. (2004). Stages in the development of Parkinson's disease-related pathology. Cell Tissue Res 318, 121-134.

Brundin, P., and Melki, R. (2017). Prying into the Prion Hypothesis for Parkinson's Disease. J Neurosci 37, 9808-9818.

Chartier-Harlin, M.C., Kachergus, J., Roumier, C., Mouroux, V., Douay, X., Lincoln, S., Levecque, C., Larvor, L., Andrieux, J., Hulihan, M., et al. (2004). Alpha-synuclein locus duplication as a cause of familial Parkinson's disease. Lancet 364, 1167-1169.

Desikan, R.S., Segonne, F., Fischl, B., Quinn, B.T., Dickerson, B.C., Blacker, D., Buckner, R.L., Dale, A.M., Maguire, R.P., Hyman, B.T., et al. (2006). An automated labeling system for

subdividing the human cerebral cortex on MRI scans into gyral based regions of interest. Neuroimage 31, 968-980.

Dickson, D.W., Braak, H., Duda, J.E., Duyckaerts, C., Gasser, T., Halliday, G.M., Hardy, J., Leverenz, J.B., Del Tredici, K., Wszolek, Z.K., and Litvan, I. (2009). Neuropathological assessment of Parkinson's disease: refining the diagnostic criteria. Lancet Neurol 8, 1150-1157.

Gonzalez-Rodriguez, P., Zampese, E., and Surmeier, D.J. (2020). Selective neuronal vulnerability in Parkinson's disease. Prog Brain Res 252, 61-89.

Du, T. T., Wang, L., Duan, C. L., Lu, L. L., Zhang, J. L., Gao, G., ... & Yang, H. (2015). GBA deficiency promotes SNCA/α-synuclein accumulation through autophagic inhibition by inactivated PPP2A. Autophagy, 11(10), 1803-1820

Raj, A., LoCastro, E., Kuceyeski, A., Tosun, D., Relkin, N., Weiner, M., et al. (2015). Network diffusion model of progression predicts longitudinal patterns of atrophy and metabolism in Alzheimer's disease. Cell Rep. 10, 359–369. doi: 10.1016/j.celrep.2014.12.034

Henderson, M. X., Cornblath, E. J., Darwich, A., Zhang, B., Brown, H., Gathagan, R. J., et al. (2019). Spread of α-synuclein pathology through the brain connectome is modulated by selective vulnerability and predicted by network analysis. Nat. Neurosci. 22:1248. doi: 10.1038/s41593-019-0457-5

Weickenmeier, J., Kuhl, E., and Goriely, A. (2018a). Multiphysics of prionlike diseases: Progression and atrophy. Physical review letters, 121(15):158101.

Newman, M. (2010). Networks: an introduction. Oxford university press.

Britton, T. (2020). Epidemic models on social networks—With inference. Statistica Neerlandica, 74(3), 222-241.

Di Stefano B, Fuks H, Lawniczak AT. Object-Oriented Implementation of CA-LGCA Modelling Applied to the Spread of Epidemics. 2000 Canadian Conference on Electrical and Computer Engineering, IEEE. 2000;1:26–31.

Frias-Martinez, E., Williamson, G., and Frias-Martinez, V. (2011). An agent-based model of epidemic spread using human mobility and social network information. In Privacy, Security, Risk and Trust (PASSAT) and 2011 IEEE Third Inernational Conference on Social Computing (SocialCom), 2011 IEEE Third International Conference on, pages 57 64. IEEE.

Zheng, Y. Q., Zhang, Y., Yau, Y., Zeighami, Y., Larcher, K., Misic, B., & Dagher, A. (2019). Local vulnerability and global connectivity jointly shape neurodegenerative disease propagation. PLoS biology, 17(11), e3000495.

Roohi Mohammad and Fatima Mubarak (2019). Neuroimaging in Parkinson Disease, Parkinson's Disease and Beyond - A Neurocognitive Approach, Sara Palermo, Mario Stanziano and Rosalba Morese, IntechOpen, DOI: 10.5772/intechopen.82308.

Politis, M. (2014). Neuroimaging in Parkinson disease: from research setting to clinical practice. Nature Reviews Neurology, 10(12), 708.

McCarthy, J., Collins, D. L., & Ducharme, S. (2018). Morphometric MRI as a diagnostic biomarker of frontotemporal dementia: A systematic review to determine clinical applicability. NeuroImage: Clinical, 20, 685-696

Ad-Dab'bagh Y, Singh V, Robbins S, Lerch J, Lyttelton O, Fombonne E, Evans AC. Native space cortical thickness measurement and the absence of correlation to cerebral volume. In: Zilles K, editor. Proceedings of the 11th Annual Meeting of the Organization for Human Brain Mapping; Toronto: 2005.

Pereira, J. B., Svenningsson, P., Weintraub, D., Brønnick, K., Lebedev, A., Westman, E., & Aarsland, D. (2014). Initial cognitive decline is associated with cortical thinning in early Parkinson disease. Neurology, 82(22), 2017-2025.

Fonov, V., Evans, A., McKinstry, R., Almli, C., Collins, D., 2009. Unbiased nonlinear average age-appropriate brain templates from birth to adulthood. NeuroImage, Organization for Human Brain Mapping 2009 Annual Meeting 47, S102.

Fonov, V., Evans, A.C., Botteron, K., Almli, C.R., McKinstry, R.C., Collins, D.L., 2011. Unbiased average age-appropriate atlases for pediatric studies. NeuroImage 54, 313–327.

Lin, C. H., Chen, C. M., Lu, M. K., Tsai, C. H., Chiou, J. C., Liao, J. R., & Duann, J. R. (2013). VBM reveals brain volume differences between Parkinson's disease and essential tremor patients. Frontiers in human neuroscience, 7, 247

Borghammer, P., Østergaard, K., Cumming, P., Gjedde, A., Rodell, A., Hall, N., & Chakravarty, M. M. (2010). A deformation-based morphometry study of patients with early-stage Parkinson's disease. European journal of neurology, 17(2), 314-320.

Park, B. Y., Byeon, K., & Park, H. (2019). FuNP (fusion of neuroimaging preprocessing) pipelines: a fully automated preprocessing software for functional magnetic resonance imaging. Frontiers in neuroinformatics, 13, 5.

Madabhushi, A., & Udupa, J. K. (2006). New methods of MR image intensity standardization via generalized scale. Medical physics, 33(9), 3426-3434.

Markello, R. D., Shafiei, G., Tremblay, C., Postuma, R. B., Dagher, A., & Miŝić, B. (2020). Integrated morphometric, molecular, and clinical characterization of Parkinson's disease pathology. BioRxi

Martins, R., Oliveira, F., Moreira, F., Moreira, A. P., Abrunhosa, A., Januário, C., & Castelo-Branco, M. (2021). Automatic classification of idiopathic Parkinson's disease and atypical Parkinsonian syndromes combining [11C] raclopride PET uptake and MRI grey matter morphometry. Journal of neural engineering, 18(4), 046037.

Zeighami, Y., Fereshtehnejad, S. M., Dadar, M., Collins, D. L., Postuma, R. B., & Dagher, A. (2019). Assessment of a prognostic MRI biomarker in early de novo Parkinson's disease. NeuroImage: Clinical, 24, 101986.

Camicioli, R., Gee, M., Bouchard, T. P., Fisher, N. J., Hanstock, C. C., Emery, D. J., & Martin, W. W. (2009). Voxel-based morphometry reveals extra-nigral atrophy patterns associated with dopamine refractory cognitive and motor impairment in parkinsonism. Parkinsonism & related disorders, 15(3), 187-195.

Nagano-Saito, A., Washimi, Y., Arahata, Y., Kachi, T., Lerch, J. P., Evans, A. C., ... & Ito, K. (2005). Cerebral atrophy and its relation to cognitive impairment in Parkinson disease. Neurology, 64(2), 224-229

Cui, X., Li, L., Yu, L., Xing, H., Chang, H., Zhao, L., ... & Dong, C. (2020). Gray Matter Atrophy in Parkinson's Disease and the Parkinsonian Variant of Multiple System Atrophy: A Combined ROI-and Voxel-Based Morphometric Study. Clinics, 75.

Hawrylycz, M.J., Lein, E.S., Guillozet-Bongaarts, A.L., Shen, E.H., Ng, L., Miller, J.A., van de Lagemaat, L.N., Smith, K.A., Ebbert, A., Riley, Z.L., et al. (2012). An anatomically comprehensive atlas of the adult human brain transcriptome. Nature 489, 391-399.

Henrich, M.T., Geibl, F.F., Lakshminarasimhan, H., Stegmann, A., Giasson, B.I., Mao, X., Dawson, V.L., Dawson, T.M., Oertel, W.H., and Surmeier, D.J. (2020). Determinants of seeding and spreading of alpha-synuclein pathology in the brain. Sci Adv 6.

Ibanez, P., Bonnet, A.M., Debarges, B., Lohmann, E., Tison, F., Pollak, P., Agid, Y., Durr, A., and Brice, A. (2004). Causal relation between alpha-synuclein gene duplication and familial Parkinson's disease. Lancet 364, 1169-1171.

Keuken, M.C., Bazin, P.L., Crown, L., Hootsmans, J., Laufer, A., Muller-Axt, C., Sier, R., van der Putten, E.J., Schafer, A., Turner, R., and Forstmann, B.U. (2014). Quantifying inter-individual anatomical variability in the subcortex using 7 T structural MRI. Neuroimage 94, 40-46.

Kordower, J.H., Chu, Y., Hauser, R.A., Freeman, T.B., and Olanow, C.W. (2008). Lewy body-like pathology in long-term embryonic nigral transplants in Parkinson's disease. Nat Med 14, 504-506.

La Joie, R., Perrotin, A., Barre, L., Hommet, C., Mezenge, F., Ibazizene, M., Camus, V., Abbas, A., Landeau, B., Guilloteau, D., et al. (2012). Region-specific hierarchy between atrophy, hypometabolism, and beta-amyloid (Abeta) load in Alzheimer's disease dementia. J Neurosci 32, 16265-16273.

Li, J.Y., Englund, E., Holton, J.L., Soulet, D., Hagell, P., Lees, A.J., Lashley, T., Quinn, N.P., Rehncrona, S., Bjorklund, A., et al. (2008). Lewy bodies in grafted neurons in subjects with Parkinson's disease suggest host-to-graft disease propagation. Nat Med 14, 501-503.

Liu, B., Fang, F., Pedersen, N.L., Tillander, A., Ludvigsson, J.F., Ekbom, A., Svenningsson, P., Chen, H., and Wirdefeldt, K. (2017). Vagotomy and Parkinson disease: A Swedish register-based matched-cohort study. Neurology 88, 1996-2002.

Luk, K.C., Kehm, V., Carroll, J., Zhang, B., O'Brien, P., Trojanowski, J.Q., and Lee, V.M. (2012a). Pathological alpha-synuclein transmission initiates Parkinson-like neurodegeneration in nontransgenic mice. Science 338, 949-953.

Luk, K.C., Kehm, V.M., Zhang, B., O'Brien, P., Trojanowski, J.Q., and Lee, V.M. (2012b). Intracerebral inoculation of pathological alpha-synuclein initiates a rapidly progressive neurodegenerative alpha-synucleinopathy in mice. J Exp Med 209, 975-986.

Marek, K., Chowdhury, S., Siderowf, A., Lasch, S., Coffey, C.S., Caspell-Garcia, C., Simuni, T., Jennings, D., Tanner, C.M., Trojanowski, J.Q., et al. (2018). The Parkinson's progression markers initiative (PPMI) - establishing a PD biomarker cohort. Ann Clin Transl Neurol 5, 1460-1477.

Masuda-Suzukake, M., Nonaka, T., Hosokawa, M., Oikawa, T., Arai, T., Akiyama, H., Mann, D.M., and Hasegawa, M. (2013). Prion-like spreading of pathological alpha-synuclein in brain. Brain 136, 1128-1138.

Pandya, S., Zeighami, Y., Freeze, B., Dadar, M., Collins, D.L., Dagher, A., and Raj, A. (2019). Predictive model of spread of Parkinson's pathology using network diffusion. Neuroimage 192, 178-194.

Peng, C., Trojanowski, J.Q., and Lee, V.M. (2020). Protein transmission in neurodegenerative disease. Nat Rev Neurol 16, 199-212.

Rey, N.L., George, S., Steiner, J.A., Madaj, Z., Luk, K.C., Trojanowski, J.Q., Lee, V.M., and Brundin, P. (2018). Spread of aggregates after olfactory bulb injection of alpha-synuclein fibrils is associated with early neuronal loss and is reduced long term. Acta Neuropathol 135, 65-83.

Rey, N.L., Steiner, J.A., Maroof, N., Luk, K.C., Madaj, Z., Trojanowski, J.Q., Lee, V.M., and Brundin, P. (2016). Widespread transneuronal propagation of alpha-synucleinopathy triggered in olfactory bulb mimics prodromal Parkinson's disease. J Exp Med 213, 1759-1778.

Spillantini, M.G., Schmidt, M.L., Lee, V.M., Trojanowski, J.Q., Jakes, R., and Goedert, M. (1997). Alpha-synuclein in Lewy bodies. Nature 388, 839-840.

Surmeier, D.J., Obeso, J.A., and Halliday, G.M. (2017). Selective neuronal vulnerability in Parkinson disease. Nat Rev Neurosci 18, 101-113.

Svensson, E., Horvath-Puho, E., Thomsen, R.W., Djurhuus, J.C., Pedersen, L., Borghammer, P., and Sorensen, H.T. (2015). Vagotomy and subsequent risk of Parkinson's disease. Ann Neurol 78, 522-529.

Tremblay, C., Abbasi, N., Zeighami, Y., Yau, Y., Dadar, M., Rahayel, S., and Dagher, A. (2020). Sex effects on brain structure in de novo Parkinson's disease: a multimodal neuroimaging study. Brain 143, 3052-3066.

Watts, J.C., Giles, K., Oehler, A., Middleton, L., Dexter, D.T., Gentleman, S.M., DeArmond, S.J., and Prusiner, S.B. (2013). Transmission of multiple system atrophy prions to transgenic mice. Proc Natl Acad Sci U S A 110, 19555-19560.

Yau, Y., Zeighami, Y., Baker, T.E., Larcher, K., Vainik, U., Dadar, M., Fonov, V.S., Hagmann, P., Griffa, A., Misic, B., et al. (2018). Network connectivity determines cortical thinning in early Parkinson's disease progression. Nat Commun 9, 12.

Zeighami, Y., Ulla, M., Iturria-Medina, Y., Dadar, M., Zhang, Y., Larcher, K.M., Fonov, V., Evans, A.C., Collins, D.L., and Dagher, A. (2015). Network structure of brain atrophy in de novo Parkinson's disease. Elife 4.

Aharon-Peretz, J., Rosenbaum, H., & Gershoni-Baruch, R. (2004). Mutations in the Glucocerebrosidase Gene and Parkinson′s Disease in Ashkenazi Jews. *New England Journal of Medicine*, *351*(19), 1972–1977. https://doi.org/10.1056/NEJMoa033277

Braak, H., Tredici, K. D., Rüb, U., de Vos, R. A. I., Jansen Steur, E. N. H., & Braak, E. (2003). Staging of brain pathology related to sporadic Parkinson′s disease. *Neurobiology of Aging*, *24*(2), 197–211. https://doi.org/10.1016/S0197-4580(02)00065-9

Brundin, P., & Melki, R. (2017). Prying into the Prion Hypothesis for Parkinson′s Disease. *The Journal of Neuroscience*, *37*(41), 9808–9818. https://doi.org/10.1523/JNEUROSCI.1788-16.2017

Campêlo, C. L. das C., & Silva, R. H. (2017). Genetic Variants in SNCA and the Risk of Sporadic Parkinson′s Disease and Clinical Outcomes: A Review. *Parkinson′s Disease*, *2017*, 1–11. https://doi.org/10.1155/2017/4318416

Laansma, M. A., Bright, J. K., Al-Bachari, S., Anderson, T. J., Ard, T., Assogna, F., Baquero, K. A., Berendse, H. W., Blair, J., Cendes, F., Dalrymple-Alford, J. C., de Bie, R. M. A., Debove, I., Dirkx, M. F., Druzgal, J., Emsley, H. C. A., Garraux, G., Guimarães, R. P., Gutman, B. A., … van der Werf, Y. D. (2020). *An International Multicenter Analysis of Brain Structure across Clinical Stages of Parkinson′s Disease: The ENIGMA-Parkinson′s Study* [Preprint]. Neurology. https://doi.org/10.1101/2020.04.28.20072710

Luk, K. C., Kehm, V. M., Zhang, B., O′Brien, P., Trojanowski, J. Q., & Lee, V. M. Y. (2012). Intracerebral inoculation of pathological α-synuclein initiates a rapidly progressive neurodegenerative α-synucleinopathy in mice. *Journal of Experimental Medicine*, *209*(5), 975–986. https://doi.org/10.1084/jem.20112457

Luna, E., Decker, S. C., Riddle, D. M., Caputo, A., Zhang, B., Cole, T., Caswell, C., Xie, S. X., Lee, V. M. Y., & Luk, K. C. (2018). Differential α-synuclein expression contributes to selective vulnerability of hippocampal neuron subpopulations to fibril-induced toxicity. *Acta Neuropathologica*, *135*(6), 855–875. https://doi.org/10.1007/s00401-018-1829-8

Miraglia, F., Ricci, A., Rota, L., & Colla, E. (2018). Subcellular localization of alpha-synuclein aggregates and their interaction with membranes. *Neural Regeneration Research*, *13*(7), 1136. https://doi.org/10.4103/1673-5374.235013

Otto, S. A., Kadin, M., Casini, M., Torres, M. A., & Blenckner, T. (2018). A quantitative framework for selecting and validating food web indicators. *Ecological Indicators*, *84*, 619–631. https://doi.org/10.1016/j.ecolind.2017.05.045

Pandya, S., Zeighami, Y., Freeze, B., Dadar, M., Collins, D. L., Dagher, A., & Raj, A. (2019). Predictive model of spread of Parkinson′s pathology using network diffusion. *NeuroImage*, *192*, 178–194. https://doi.org/10.1016/j.neuroimage.2019.03.001

Riboldi, G. M., & Di Fonzo, A. B. (2019). GBA, Gaucher Disease, and Parkinson′s Disease: From Genetic to Clinic to New Therapeutic Approaches. *Cells*, *8*(4), 364. https://doi.org/10.3390/cells8040364

Stanley, M. L., Moussa, M. N., Paolini, B. M., Lyday, R. G., Burdette, J. H., & Laurienti, P. J. (2013). Defining nodes in complex brain networks. *Frontiers in Computational Neuroscience*, *7*. https://doi.org/10.3389/fncom.2013.00169

Surmeier, D. J., Obeso, J. A., & Halliday, G. M. (2017). Selective neuronal vulnerability in Parkinson disease. *Nature Reviews Neuroscience*, *18*(2), 101–113. https://doi.org/10.1038/nrn.2016.178

Tremblay, C., Rahayel, S., Vo, A., Morys, F., Shafiei, G., Markello, R. D., Gan-Or, Z., Misic, B., & Dagher, A. (2021). *Brain atrophy progression in Parkinson′s disease is shaped by connectivity and local vulnerability* [Preprint]. Pathology. https://doi.org/10.1101/2021.06.08.21258321

Weickenmeier, J., Kuhl, E., & Goriely, A. (2018). Multiphysics of Prionlike Diseases: Progression and Atrophy. *Physical Review Letters*, *121*(15), 158101. https://doi.org/10.1103/PhysRevLett.121.158101